Published for SISSA by Springer

Received: June 24, 2025
Accepted: September 19, 2025
Published: November 13, 2025

Study of $\langle p_{\mathrm{T}} \rangle$ and its higher moments, and extraction of the speed of sound in Pb-Pb collisions with ALICE

The ALICE collaboration

I.J. Abualrob et al.
Full author list at the end of the paper

E-mail: ALICE-publications@cern.ch

Abstract: Ultrarelativistic heavy-ion collisions produce a state of hot and dense strongly interacting QCD matter called quark-gluon plasma (QGP). On an event-by-event basis, the volume of the QGP in ultracentral collisions is mostly constant, while its total entropy can vary significantly due to quantum fluctuations, leading to variations in the temperature of the system. Exploiting this unique feature of ultracentral collisions allows for the interpretation of the correlation of the mean transverse momentum ($\langle p_{\mathrm{T}} \rangle$) of produced charged hadrons and the number of charged hadrons as a measure for the speed of sound, c_{s}. This speed is related to the rate at which compression waves travel in the QGP and is determined by fitting the relative increase in $\langle p_{\mathrm{T}} \rangle$ with respect to the relative change in the average charged-particle density ($\langle \mathrm{d}N_{\mathrm{ch}}/\mathrm{d}\eta \rangle$) measured at mid-rapidity. This study reports the event-average $\langle p_{\mathrm{T}} \rangle$ of charged particles as well as the variance, skewness, and kurtosis of the event-by-event transverse momentum per charged particle ($[p_{\mathrm{T}}]$) distribution in ultracentral Pb-Pb collisions at a center-of-mass energy of 5.02 TeV per nucleon pair using the ALICE detector. Different centrality estimators based on charged-particle multiplicity or the transverse energy of the event are used to select ultracentral collisions. By ensuring a pseudorapidity gap between the region used to define the centrality and the region used to perform the measurement, the influence of biases and their potential effects on the rise of the mean transverse momentum is tested. The measured c_{s}^2 is found to strongly depend on the exploited centrality estimator and ranges between 0.1146±0.0028 (stat.)±0.0065 (syst.) and 0.4374±0.0006 (stat.)±0.0184 (syst.)

https://doi.org/10.1007/JHEP11(2025)076

JHEP11(2025)076

in natural units. The self-normalized variance shows a steep decrease towards ultracentral collisions, while the self-normalized skewness variables show a maximum, followed by a fast decrease. These non-Gaussian features are understood in terms of the vanishing of the impact-parameter fluctuations contributing to the event-to-event $[p_{\mathrm{T}}]$ distribution.

Keywords: Heavy Ion Experiments, Particle Correlations and Fluctuations, Quark Gluon Plasma

ArXiv ePrint: 2506.10394

Contents

1 Introduction

It is well established that collisions of heavy ions at ultrarelativistic energies produce a quark-gluon plasma (QGP) [1–7], a state of matter in which quarks and gluons are deconfined and not bound inside hadrons. The QGP formed in a collision undergoes a quick phase of thermalization [8] before it expands as a relativistic hydrodynamic fluid. The hydrodynamic description of the QGP stands as one of the great successes in developing an effective theory of many-body quantum chromodynamics (QCD) at high temperatures [6, 9, 10]. As the system expands, both its energy and entropy density decrease and eventually the system undergoes a phase transition as a consequence of which hadrons are formed [11, 12].

It has been suggested that the QGP phase can be studied by measuring the mean transverse momentum ($\langle p_T\rangle$) of the produced hadrons in ultracentral Pb-Pb collisions [13–15]. On an event-by-event basis, the volume of the QGP in ultracentral collisions is mostly constant, while the charged-particle multiplicity (N_{ch}) can vary significantly [13]. The increase of the charged-particle multiplicity is interpreted as fluctuations in the entropy, which is created early in the collision primarily through interactions of the sea gluons of the colliding nuclei [16]. As the volume is mostly constant, the corresponding rise in the entropy density (s) leads to higher temperatures (T), as the entropy density is approximately proportional to T^3 for the QCD equation of state of high temperature deconfined matter [17].

The dependence of the pressure, P, of the QGP on the energy density, ϵ, is encoded in the corresponding QCD equation of state $P = P(\varepsilon)$ [18]. The equation of state determines how gradients in the energy density profile give rise to pressure gradients [6]. These gradients of pressure accelerate fluid elements, and facilitate a collective expansion. A fundamental quantity that characterizes the expansion of hot dense matter is the speed of sound, denoted as c_s, which is the speed at which a compression wave travels in a medium. In a relativistic fluid, it is given by $c_s^2 = \mathrm{d}\,P/\mathrm{d}\,\epsilon = \mathrm{d}\ln T/\mathrm{d}\ln s$ [19]. Assuming that the increase in the average transverse momentum is solely due to temperature fluctuations, and the charged-particle multiplicity is proportional to the entropy density [15, 20] of the QGP, the speed of sound can be determined experimentally [21, 22] as $c_s^2 = \mathrm{d}\ln\langle p_T\rangle/\mathrm{d}\ln N_{ch}$. However, this approach does not account for the contribution to $\langle p_T\rangle$ from radial flow, which is proportional to the inverse size, $1/R$, of the overlap region [23, 24] — radial flow pushes the $\langle p_T\rangle$ to higher values with increasing centrality [25].

The study of the event-by-event distribution of transverse momentum per charged particle, denoted by $[p_T]$, in ultracentral collisions serves as a tool to probe quantum fluctuations of the initial stage of the collision [26, 27]. For collisions with the same N_{ch}, $[p_T]$ fluctuations arise from impact parameter (b) variations and from a quantum nature. Quantum fluctuations originate from the event-to-event positions of the nucleons when colliding and the partonic content of the nucleons [23, 28]. At a fixed-impact parameter, $[p_T]$ fluctuations are small and approximately Gaussian distributed but a non-zero skewness is predicted to be driven by event-to-event impact-parameter fluctuations. In particular, ref. [26] predicts a rapid increase of the skewness for N_{ch} beyond the *knee* ($N_{ch,knee}$) marking the rapid decline of the multiplicity distribution for central collisions, followed by a fast decrease. The multiplicity $N_{ch,knee}$ at the knee is defined as the average multiplicity of collisions at $b = 0$.

The ATLAS collaboration has reported the measurement of the higher-order moments of $[p_T]$ in central collisions [22]. In particular, the $Var([p_T])$ features a steep decrease towards the ultracentral collision regime. This striking phenomenon is described in terms of the disappearance of the impact-parameter fluctuations in collisions with the largest multiplicity. Additionally, such observations can only be explained by the presence of a thermalized medium early in the collision, and can serve as a probe of the transport properties of the QGP relying on isotropic expansion instead of anisotropic flow [27]. The ALICE collaboration previously measured the skewness and kurtosis of the event-by-event mean transverse momentum in wide bins of average charged-particle density ($\langle \mathrm{d}N_{ch}/\mathrm{d}\eta\rangle$) across different systems [29]. In this article, the study of the higher-order moments of $[p_T]$ is restricted to the ultracentral Pb-Pb collisions at $\sqrt{s_{NN}} = 5.02$ TeV.

This study reports the measurement of the normalized variance (k_2), normalized skewness (k_3), standardized skewness ($\gamma_{\langle[p_T]\rangle}$), intensive skewness ($\Gamma_{\langle[p_T]\rangle}$), and standardized kurtosis ($\kappa_{\langle[p_T]\rangle}$) of the event-by-event $[p_T]$ distribution, as well as the event-average $\langle p_T\rangle$ and the event-average $\langle \mathrm{d}N_{ch}/\mathrm{d}\eta\rangle$ in ultracentral collisions divided into narrow centrality intervals. The data set corresponds to those collisions with the top 0–5% highest charged-particle multiplicities and top 0–5% highest transverse energy. In this article, 'ultracentral collisions' denotes the 0–0.1% or smaller fractions of these events with the highest charged-particle multiplicities or transverse energy. A primary purpose of this study is to compare results obtained using charged-particle multiplicity (N_{ch}) centrality estimators with those using transverse-energy (E_T) centrality estimators. Furthermore, different kinematic selections on the particles used to define centrality are employed, as it has been found that the definition of the centrality estimator used to measure the $\langle p_T\rangle$ and $\langle \mathrm{d}N_{ch}/\mathrm{d}\eta\rangle$ can influence the extracted values of c_s^2 [14, 30]. Some of the centrality estimators feature a different choice of pseudorapidity gap with respect to the region used to determine $\langle p_T\rangle$ as a function of $\langle \mathrm{d}N_{ch}/\mathrm{d}\eta\rangle$. This is particularly relevant to select high-multiplicity events (ultracentral collisions) with a suppressed contribution of particles from jet fragmentation.

This article is organized as follows. The ALICE experimental setup is described in section 2, focusing on the detectors which are relevant to the presented measurements. Section 3 discusses the analyzed data samples, the event and track-selection criteria, the centrality-estimator definitions, and the analysis techniques to measure the higher-order moments of $[p_{\mathrm{T}}]$ and the $\langle p_{\mathrm{T}}\rangle$ versus $\langle \mathrm{d}N_{\mathrm{ch}}/\mathrm{d}\eta\rangle$ correlation. Section 3 also outlines the estimation of systematic uncertainties. The results are presented and discussed in section 4, including comparisons to Monte Carlo model predictions. Finally, section 5 gives the summary and draws the conclusions.

2 Experimental setup

A detailed description of the ALICE detector and its performance is provided in refs. [31, 32]. Relevant detectors for this study include the V0 detector [33], the Inner Tracking System (ITS) [34], the Time Projection Chamber (TPC) [35], and the Zero Degree Calorimeters (ZDC) [36, 37].

The V0 detector is composed of two scintillator arrays placed along the beam axis (z) on each side of the interaction point ($z = 0$): V0A at $z = 340$ cm and V0C at $z = -90$ cm. These arrays cover the pseudorapidity regions $2.8 < \eta < 5.1$ (V0A) and $-3.7 < \eta < -1.7$ (V0C). The V0 detector provides the minimum bias trigger, which is defined by the requirement of signals in both V0A and V0C detectors in coincidence with a particle bunch crossing corresponding to a beam-beam collision [33]. The V0 signals are proportional to the total charge deposited in the scintillators, which correlates with the charged-particle multiplicity in the V0 acceptance. The V0 detector is also used for centrality estimation [38] and for removing beam induced (beam-gas) background based on timing information.

The ITS and TPC detectors are located within a solenoid that provides a maximum 0.5 T magnetic field parallel to the beam axis. The ITS is a six-layer silicon detector [34], surrounding the beam pipe. The two innermost layers comprise the Silicon Pixel Detector (SPD), located at average distances of 3.9 and 7.6 cm from the beam line with a pseudorapidity coverage of $|\eta| < 2$ and $|\eta| < 1.4$, respectively. The track segments joining hits in the two SPD layers are called *tracklets*. The number of tracklets ($N_{\mathrm{tracklets}}$) is used to estimate the number of primary charged particles produced in the collisions. The Silicon Drift Detector (SDD) comprises the next two layers of the ITS. In addition to tracking, the SDD provide charged-particle identification via the measurement of the specific ionization energy loss ($\mathrm{d}E/\mathrm{d}x$). The TPC is the main tracking detector, covering the pseudorapidity range $|\eta| < 0.9$ with full azimuthal coverage. By measuring drift time, the TPC provides three-dimensional space-point information for each charged track, with up to 159 space points. Tracks originating from the primary vertex can be reconstructed down to $p_{\mathrm{T}} \sim 100\,\mathrm{MeV}/c$ [32]. Charged-particle multiplicity (N_{ch}) and a proxy for the transverse energy (E_{T}) measured with the TPC detector are used to estimate the collisions centrality. Transverse energy is quantified as the summed transverse mass ($m_{\mathrm{T}} = \sqrt{p_{\mathrm{T}}^2 + m_\pi^2}$), assuming the pion mass for all particles.

The ZDC measures the energy of the spectator nucleons in the forward direction, providing a direct estimate of the average number of participating nucleons ($\langle N_{\mathrm{part}}\rangle$) in the collisions. The $\langle N_{\mathrm{part}}\rangle$ calculation is valid for central collisions (0–5%) where the contribution from nuclear fragments that escape detection by the ZDC is negligible [38]. The neutron (ZNC

JHEP11(2025)076

and ZNA) calorimeters are placed at zero degrees with respect to the LHC beam axis to detect forward going neutral particles at pseudorapidities $|\eta| > 8.8$, while the proton (ZPC and ZPA) calorimeters are located externally to the outgoing beam vacuum tube. In this study, the ZDC detector is only used to estimate the centrality dependent $\langle N_{\mathrm{part}} \rangle$ [38].

3 Analysis procedure

Event and track selection

The present study uses data from Pb-Pb collisions at $\sqrt{s_{\mathrm{NN}}} = 5.02\,\mathrm{TeV}$ collected during the Run 2 data-taking period of the LHC in 2018. The primary-vertex position is reconstructed using information from both the TPC and ITS detectors. A $\pm 10\,\mathrm{cm}$ selection is applied to the primary-vertex position along the beam axis to ensure uniform pseudorapidity coverage in the SPD and TPC detectors at mid-rapidity. The total number of minimum bias collisions analyzed after event and vertex selections amounts to about 193 million.

This analysis uses primary charged particles, which are defined as charged particles produced directly in the collision with a mean proper lifetime τ that is larger than $1\,\mathrm{cm}/c$, or from decays of particles produced at the interaction point with τ shorter than $1\,\mathrm{cm}/c$, excluding daughters from long-lived weakly decaying hadrons and particles produced in interactions with the detector material [39]. Tracks of primary charged particles are reconstructed using the combined information from the ITS and TPC detectors. The track-selection criteria are the same as the ones used in previous studies [25], and yield the best track quality and minimal contamination from secondary particles. The reconstructed tracks are required to have a minimum ratio between crossed rows and reconstructed space points in the TPC of 0.8. The fit quality for the ITS and TPC track points must satisfy $\chi^2_{\mathrm{ITS}}/N_{\mathrm{hits}} < 36$ and $\chi^2_{\mathrm{TPC}}/N_{\mathrm{clusters}} < 4$, where N_{hits} and N_{clusters} are the number of hits in the ITS and the number of reconstructed space points in the TPC associated to a track, respectively. To limit the contamination from secondary particles, the distance-of-closest approach (DCA) to the primary vertex in the transverse plane has to satisfy the p_{T}-dependent selection: $|\mathrm{DCA}_{xy}| < A + B \cdot p_{\mathrm{T}}^{C}$, with $A = 0.0182\,\mathrm{cm}$, $B = 0.035\,\mathrm{cm}$, and $C = -1.01$. The p_{T} is the numerical value of the transverse momentum in units of GeV/c. A 2 cm selection is also applied to the DCA along the z axis. Finally, primary charged particles are measured in the kinematic range $|\eta| \leq 0.8$ and $0.15 \leq p_{\mathrm{T}} < 50\,\mathrm{GeV}/c$.

Selecting ultracentral collisions

A primary objective of this analysis is to investigate the recently reported dependence of the measured c_{s} on the acceptance, kinematic selections, and the observable used to determine the collision centrality [14, 30]. Table 1 summarizes the different centrality estimators, including the kinematic selections on particles used for centrality estimation and for the measurement of $\langle p_{\mathrm{T}} \rangle$ and $\langle \mathrm{d}N_{\mathrm{ch}}/\mathrm{d}\eta \rangle$. Centrality estimators based on the number of SPD tracklets include particles with transverse momenta starting from approximately $0.03\,\mathrm{GeV}/c$ and have no upper p_{T} limit. In contrast, the centrality estimators using the number of charged particles reconstructed with the TPC are constrained to $0.15 \leq p_{\mathrm{T}} < 50\,\mathrm{GeV}/c$. This also applies to the E_{T}-based centrality estimators.

JHEP11(2025)076

Observable	Label	Centrality estimation	$\langle p_T \rangle$ and $\langle dN_{ch}/d\eta \rangle$	Minimum $\lvert\Delta\eta\rvert$
N_{ch} in TPC	I	$\lvert\eta\rvert \leq 0.8$	$\lvert\eta\rvert \leq 0.8$	0
	II	$0.5 \leq \lvert\eta\rvert < 0.8$	$\lvert\eta\rvert \leq 0.3$	0.2
E_T in TPC	III	$\lvert\eta\rvert \leq 0.8$	$\lvert\eta\rvert \leq 0.8$	0
	IV	$0.5 \leq \lvert\eta\rvert < 0.8$	$\lvert\eta\rvert \leq 0.3$	0.2
$N_{tracklets}$ in SPD	V	$\lvert\eta\rvert \leq 0.8$	$\lvert\eta\rvert \leq 0.8$	0
	VI	$0.5 \leq \lvert\eta\rvert < 0.8$	$\lvert\eta\rvert \leq 0.3$	0.2
	VII	$0.3 < \lvert\eta\rvert < 0.6$	$\lvert\eta\rvert \leq 0.3$	0
	VIII	$0.7 \leq \lvert\eta\rvert < 1$	$\lvert\eta\rvert \leq 0.3$	0.4
N_{ch} in V0	IX	$-3.7 < \eta < -1.7$ and $2.8 < \eta < 5.1$	$\lvert\eta\rvert \leq 0.8$	0.9

Table 1. The columns, from left to right, present: the observable used for centrality estimation, the label identifying each estimator in the figures, the pseudorapidity interval used to measure event activity for centrality classification, the pseudorapidity interval used to measure $\langle p_T \rangle$ and $\langle dN_{ch}/d\eta \rangle$, and the minimum pseudorapidity gap between the centrality estimation region and the region to measure $\langle p_T \rangle$ and $\langle dN_{ch}/d\eta \rangle$. The p_T selections for charged tracks and tracklets are given in the text.

Significant autocorrelation effects are expected when the pseudorapidity intervals used for centrality estimation and for $\langle p_T \rangle$ and $\langle dN_{ch}/d\eta \rangle$ measurement completely overlap. This occurs when event activity for centrality assessment is quantified in $|\eta| \leq 0.8$, and $\langle p_T \rangle$ and $\langle dN_{ch}/d\eta \rangle$ are measured within the same pseudorapidity window, as represented by labels I, III, and V in table 1. Specifically, a multiplicity bias is expected with N_{ch}-based estimators, and an energy bias is expected with E_T-based estimators.

A pseudorapidity gap is introduced between the centrality estimation region and the region used for $\langle p_T \rangle$ and $\langle dN_{ch}/d\eta \rangle$ measurement. This is particularly important for suppressing the effects of particles from jet fragmentation. The fragmentation of jets into charged particles with intermediate to high p_T can increase both $\langle p_T \rangle$ and $\langle dN_{ch}/d\eta \rangle$, which may not necessarily reflect an increase in the entropy density of the QGP.

A pseudorapidity gap is introduced for centrality estimators based on the N_{ch} in TPC (II), E_T in TPC (IV), $N_{tracklets}$ in SPD (VI and VIII), and N_{ch} in V0 (IX), as defined in table 1. Notably, estimators labeled VIII and IX allow for the investigation of $\langle p_T \rangle$ and $\langle dN_{ch}/d\eta \rangle$ dependence with a wider pseudorapidity gap.

This analysis also includes a case where the pseudorapidity region for centrality estimation is adjacent to the region used for $\langle p_T \rangle$ and $\langle dN_{ch}/d\eta \rangle$ measurement. This case utilizes the $N_{tracklets}$ in the SPD detector and is labeled as VII.

Previous ALICE publications employed a phenomenological approach to extract the average number of participating nucleons, $\langle N_{part} \rangle$, relying on a Glauber Monte Carlo calculation convoluted with a negative binomial distribution (NBD) model for particle production to fit the V0 amplitude distribution [38]. In this analysis, a data-driven method is employed to measure the $\langle N_{part} \rangle$ in the 0–5% centrality interval.

Figure 1 illustrates the centrality dependence of $\langle N_{part} \rangle$, computed from the average number of spectator nucleons reaching the ZDC detector [38]. The $\langle N_{part} \rangle$ is determined

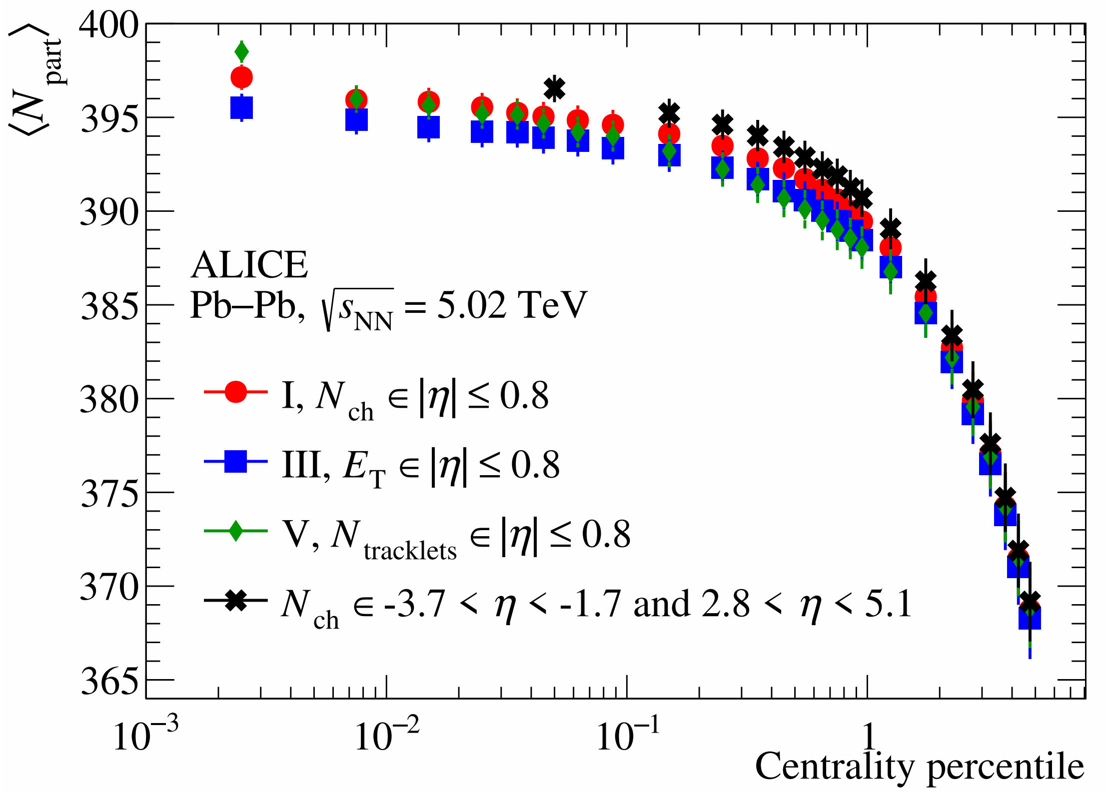

Figure 1. Average number of participating nucleons ($\langle N_{part}\rangle$) as a function of centrality percentile in Pb-Pb collisions at $\sqrt{s_{NN}} = 5.02$ TeV. Data points are shown for centrality estimators based on N_{ch}, E_T, $N_{tracklets}$ within $|\eta| \leq 0.8$, and N_{ch} within $-3.7 < \eta < -1.7$ and $2.8 < \eta < 5.1$. Uncertainty bars represent the sum of statistical and systematic uncertainties, with the latter being the dominant source. The systematic uncertainty is determined by varying the acceptance correction factors within their uncertainties and assigning the maximum deviation from the nominal N_{part} value as the systematic uncertainty.

using the following equation

$$\langle N_{part}\rangle = 2\mathrm{A} - \left(\frac{\langle E_{ZNC}\rangle}{\alpha_{ZNC}} + \frac{\langle E_{ZNA}\rangle}{\alpha_{ZNA}} + \frac{\langle E_{ZPC}\rangle}{\alpha_{ZPC}} + \frac{\langle E_{ZPA}\rangle}{\alpha_{ZPA}} \right) \Big/ E_A\,, \tag{3.1}$$

where A = 208 is the mass number of the Pb nucleus, $E_A = 2.51$ TeV is the beam energy per nucleon, $\langle E_{ZNC}\rangle$, $\langle E_{ZNA}\rangle$, $\langle E_{ZPC}\rangle$, and $\langle E_{ZPA}\rangle$ represent the neutron and proton energies deposited in the neutron and proton calorimeters on each side of the interaction point, and $\alpha_{ZNC} = 0.933 \pm 0.0165$, $\alpha_{ZNA} = 0.931 \pm 0.0164$, $\alpha_{ZPC} = 0.5 \pm 0.05$, and $\alpha_{ZPA} = 0.52 \pm 0.07$ are the corresponding corrections for detection efficiency and acceptance, calculated with Monte Carlo simulated events [40]. The uncertainties in the proton correction factors, which encompass variations in beam optics during Pb-Pb data taking in 2018, are included in the $\langle N_{part}\rangle$ estimation.

Figure 1 presents results for centrality estimators using N_{ch}, E_T, $N_{tracklets}$ within $|\eta| \leq 0.8$, and N_{ch} within $-3.7 < \eta < -1.7$ and $2.8 < \eta < 5.1$. Similar results are obtained for the other centrality estimators. The data demonstrate a consistent trend across all estimators, regardless of whether charged-particle multiplicity or transverse energy is used for event classification. The $\langle N_{\rm part}\rangle$ increases rapidly from the 4.5–5% to the 0.9–1% centrality interval and then exhibits a slight saturation for the most central collisions. The relative increase of $\langle N_{\rm part}\rangle$ in the 0–0.005% centrality interval compared to the 0.9–1% interval is approximately 1%, suggesting that the volume of the QGP remains relatively constant in the ultracentral-collision limit.

The $\langle N_{\rm part}\rangle$ values in the 0–0.1% centrality range, determined using the $E_{\rm T}$ centrality estimator, are systematically lower compared to those obtained with $N_{\rm ch}$ centrality estimators, indicating distinct selection biases. Specifically, collisions characterized by lower $\langle N_{\rm part}\rangle$ tend to exhibit lower $N_{\rm ch}$ at mid-rapidity and greater impact-parameter fluctuations. The $N_{\rm ch}$-based centrality estimators generally select higher $\langle N_{\rm part}\rangle$ values for the same centrality interval than the $E_{\rm T}$-based estimator. These selection biases are described in detail in section 4 when examining the evolution of $\langle p_{\rm T}\rangle$ as a function of the centrality estimators. Conversely, the $N_{\rm tracklets}$-based centrality estimator yields the largest $\langle N_{\rm part}\rangle$ increase from 1% to 0% centrality. Finally, the V0-based centrality estimator employs coarser binning for the most ultracentral collisions.

The estimation of $\langle N_{\rm part}\rangle$ with the V0-based centrality estimator yields a value of 388 for the 0–5% centrality class, which agrees within 1% with a calculation using a NBD-Glauber fit to the V0 amplitude distribution [41]. It is interesting to note that $\langle N_{\rm part}\rangle$ does not reach the asymptotic value of 416. This is expected, as previous calculations show the radius of the overlap region saturates at around 6 fm [13], which is below the Pb nucleus radius of 6.7 fm. Therefore, reaching the asymptotic value is not possible, as the nuclei never fully overlap in the ultracentral region explored.

Measuring $\langle p_{\rm T}\rangle$, $\langle {\rm d}N_{\rm ch}/{\rm d}\eta\rangle$, and the higher-order moments of $[p_{\rm T}]$

The speed of sound is extracted from a fit to the correlation between the normalized event-average transverse momentum, $\langle p_{\rm T}\rangle^{\rm norm} = \langle p_{\rm T}\rangle/\langle p_{\rm T}\rangle^{0\text{–}5\%}$, and the normalized event-average charged-particle density $\langle {\rm d}N_{\rm ch}/{\rm d}\eta\rangle^{\rm norm} = \langle {\rm d}N_{\rm ch}/{\rm d}\eta\rangle/\langle {\rm d}N_{\rm ch}/{\rm d}\eta\rangle^{0\text{–}5\%}$, where the normalization constants are measured in the 0–5% centrality range. Both quantities are derived from the centrality-dependent transverse-momentum spectra fully corrected for the acceptance, tracking inefficiency, and secondary-particle contamination. The spectra are measured and corrected using standard methods [25], which involve employing HIJING event simulations [42]. The generated particles are subsequently propagated through a simulation of the ALICE detector using the GEANT 3 transport code [43]. The simulated particles are reconstructed using the same algorithms as for the data. The corrections are determined using a high-multiplicity sample, specifically collisions in the 0–5% centrality interval. The tracking-inefficiency correction accounts for the particle composition of the charged-hadron spectrum. The transverse-momentum dependent fractions of charged pions, kaons, protons, and sigma baryons are used to refine the Monte Carlo-based tracking inefficiency correction [25]. The residual contamination from secondary particles (products of weak decays and particles produced from interactions with the detector material) is estimated using a data-driven approach based on a multi-template fit of the data ${\rm DCA}_{xy}$ distributions in transverse-momentum intervals. The ${\rm DCA}_{xy}$ distributions are fitted with three Monte Carlo templates representing the contribution from primary and secondary particles, with the latter originating from weak decays or from interactions with the detector material. The fraction of secondary particles amounts to 12% at $p_{\mathrm{T}} = 0.15\,\mathrm{GeV}/c$ and decreases asymptotically to about 2% at $p_{\mathrm{T}} = 3.5\,\mathrm{GeV}/c$.

The $\langle p_{\mathrm{T}}\rangle$ and $\langle \mathrm{d}N_{\mathrm{ch}}/\mathrm{d}\eta\rangle$ are derived from the p_{T} spectra in the interval $0 \leq p_{\mathrm{T}} \leq 10\,\mathrm{GeV}/c$. Prior to the calculation, an extrapolation procedure is applied to estimate the unmeasured yield in the interval between $0 \leq p_{\mathrm{T}} < 0.15\,\mathrm{GeV}/c$. The extrapolation procedure closely follows that described in refs. [44, 45], where the transverse-momentum spectra are fitted with a Boltzmann-Gibbs Blast-Wave model [46] in the interval between $0.15 \leq p_{\mathrm{T}} \leq 1.5\,\mathrm{GeV}/c$. The fit range is selected based on the χ^2/ndf criterion. The extrapolated p_{T}-integrated yield amounts to approximately 9% of the yield in the $0 \leq p_{\mathrm{T}} \leq 10\,\mathrm{GeV}/c$ interval.

The statistical uncertainty on $\langle p_{\mathrm{T}}\rangle$ and $\langle \mathrm{d}N_{\mathrm{ch}}/\mathrm{d}\eta\rangle$ is calculated by shifting each data point by a fraction of its statistical uncertainty. The fraction is randomly drawn from a Gaussian distribution with a standard deviation of 1, and new values of integrated yields and mean transverse momenta are calculated. The procedure is repeated 1000 times, and the standard deviations of $\langle p_{\mathrm{T}}\rangle$ and $\langle \mathrm{d}N_{\mathrm{ch}}/\mathrm{d}\eta\rangle$ are used as the statistical uncertainties.

The reported higher-order moments of $[p_{\mathrm{T}}]$, defined in (3.3)–(3.6), are the normalized variance ($k_2^{\mathrm{norm}} = k_2/k_2^{0\text{–}5\%}$), skewness ($k_3^{\mathrm{norm}} = k_3/k_3^{0\text{–}5\%}$), standardized skewness ($\gamma^{\mathrm{norm}}_{\langle[p_{\mathrm{T}}]\rangle} = \gamma_{\langle[p_{\mathrm{T}}]\rangle}/\gamma^{0\text{–}5\%}_{\langle[p_{\mathrm{T}}]\rangle}$), intensive skewness ($\Gamma^{\mathrm{norm}}_{\langle[p_{\mathrm{T}}]\rangle} = \Gamma_{\langle[p_{\mathrm{T}}]\rangle}/\Gamma^{0\text{–}5\%}_{\langle[p_{\mathrm{T}}]\rangle}$), and kurtosis ($\kappa^{\mathrm{norm}}_{\langle[p_{\mathrm{T}}]\rangle} = \kappa_{\langle[p_{\mathrm{T}}]\rangle}/\kappa^{0\text{–}5\%}_{\langle[p_{\mathrm{T}}]\rangle}$) as a function of $\langle \mathrm{d}N_{\mathrm{ch}}/\mathrm{d}\eta\rangle^{\mathrm{norm}}$. The self-normalized quantities provide precise measurements of the relative variations in ultracentral collisions with respect to their values in the 0–5% centrality class since the common uncertainties between the numerator and denominator cancel out.

The cumulants are genuine correlations unbiased by contributions from lower-order correlations and are related to the properties of the distribution, such as the variance, skewness, and kurtosis. The cumulants are constructed from the p_{T} correlations, $[p_{\mathrm{T}}^{(k)}]$, given by [47]

$$[p_{\mathrm{T}}^{(k)}] = \frac{\sum_{i_1 \neq \ldots \neq i_k} w_{i_1} \ldots w_{i_k} p_{\mathrm{T},i_1} \ldots p_{\mathrm{T},i_k}}{\sum_{i_1 \neq \ldots \neq i_k} w_{i_1} \ldots w_{i_k}}, \tag{3.2}$$

where the index runs over distinct k-particle tuplets, $i_1 \neq \ldots \neq i_k$, and w_i are particle weights to correct for non-uniform efficiencies of the detectors. The second-, third-, and fourth-order p_{T}-cumulants are

$$c_2 = \langle [p_{\mathrm{T}}^{(2)}]\rangle - \langle [p_{\mathrm{T}}]\rangle^2, \tag{3.3}$$

$$c_3 = \langle [p_{\mathrm{T}}^{(3)}]\rangle - 3\langle [p_{\mathrm{T}}^{(2)}]\rangle\langle [p_{\mathrm{T}}]\rangle + 2\langle [p_{\mathrm{T}}]\rangle^3, \tag{3.4}$$

$$c_4 = \langle [p_{\mathrm{T}}^{(4)}]\rangle - 4\langle [p_{\mathrm{T}}^{(3)}]\rangle\langle [p_{\mathrm{T}}]\rangle - 3\langle [p_{\mathrm{T}}^{(2)}]\rangle^2 + 12\langle [p_{\mathrm{T}}^{(2)}]\rangle\langle [p_{\mathrm{T}}]\rangle^2 - 6\langle [p_{\mathrm{T}}]\rangle^4. \tag{3.5}$$

The cumulants are then converted to their normalized, dimensionless form

$$k_2 = \frac{c_2}{\langle [p_{\mathrm{T}}^{(2)}]\rangle}, \quad k_3 = \frac{c_3}{\langle [p_{\mathrm{T}}^{(3)}]\rangle}, \quad \gamma_{\langle[p_{\mathrm{T}}]\rangle} = \frac{c_3}{c_2^{3/2}}, \quad \Gamma_{\langle[p_{\mathrm{T}}]\rangle} = \frac{c_3 \cdot \langle [p_{\mathrm{T}}]\rangle}{c_2^2}, \quad \kappa_{\langle[p_{\mathrm{T}}]\rangle} = \frac{c_4 + 3c_2^2}{c_2^2}. \tag{3.6}$$

The higher-order cumulants are measured at mid-rapidity ($|\eta| < 0.8$) and within $0.2 < p_{\mathrm{T}} < 3\,\mathrm{GeV}/c$ as a function of the event-by-event charged-particle multiplicity density and transverse energy in the same kinematic phase space. The statistical uncertainty is estimated using standard procedures [48], which employ the bootstrap method of random sampling with replacement [49].

Systematic uncertainties

This section describes the calculation of the total systematic uncertainty on the average transverse momentum, the event-by-event higher-order mean transverse-momentum cumulants, and the average charged-particle density. Two sources of systematic uncertainty are considered.

The first is due to the used vertex and track selections. The effect of selecting events based on the vertex position is studied by comparing the default results to the fully corrected $\langle p_{\mathrm{T}}\rangle^{\mathrm{norm}}$ and $\langle \mathrm{d}N_{\mathrm{ch}}/\mathrm{d}\eta\rangle^{\mathrm{norm}}$ obtained with an alternative vertex selection corresponding to ± 5 cm and for the high-order cumulants corresponding to ± 7, and ± 9 cm. The average relative systematic uncertainty is 0.02% for $\langle p_{\mathrm{T}}\rangle^{\mathrm{norm}}$ and effectively zero for $\langle \mathrm{d}N_{\mathrm{ch}}/\mathrm{d}\eta\rangle^{\mathrm{norm}}$ in the 0–5% centrality range. However, in the higher-order mean transverse-momentum cumulants analysis, it was found to be statistically insignificant based on the Barlow criterion [50]. The systematic uncertainty due to the track-selection criteria is investigated by varying the selections employed on the tracks. In particular, the minimum ratio between crossed rows and reconstructed space points in the TPC is shifted to 0.7 and 0.9 (the nominal is 0.8). The $\chi^2_{\mathrm{ITS}}/N_{\mathrm{hits}}$ is set to 25 and 49 (the nominal is 36), while the $\chi^2_{\mathrm{TPC}}/N_{\mathrm{clusters}}$ is shifted to 3 and 5 (the nominal is 4). The DCA_z selection along the beam axis is also varied to 1 and 5 cm (the nominal is 2 cm). The relative systematic uncertainty for $\langle p_{\mathrm{T}}\rangle^{\mathrm{norm}}$ is 0.21% in the most central collisions and decreases with decreasing centrality. For the higher-order cumulants, the quality of the reconstructed tracks is varied by increasing the number of TPC space points from a default of 70 to 80 and 90, which leads to less than 0.5% variation for the results based on mid-rapidity centrality estimators and less than a 3% variation for the results based on forward centrality estimator. Additionally, a different track type is considered, which includes additional tracks without hits in the innermost layer of the ITS to recover a uniform distribution as a function of φ and η. This leads to a negligible variation for mid-rapidity centrality estimators and around 3% for the forward centrality estimator. Finally, the variations of the DCA in the longitudinal and transverse planes lead to differences $< 1\%$ in the mid-rapidity-based cases and $< 2\%$ and $< 3\%$, respectively, in the forward-based cases. The systematic uncertainty is quantified as: $\mathrm{Unc} = 1 - (X_{\mathrm{var}}/X_{\mathrm{nom}})/(X^{0\text{–}5\%}_{\mathrm{var}}/X^{0\text{–}5\%}_{\mathrm{nom}})$, where X_{nom} represents the nominal observable (average transverse momentum or higher-order cumulants), and X_{var} is the value of the same observable for a particular variation. The second source of systematic uncertainty, which is only considered for the event-averaged mean transverse momentum, is the choice of the Boltzmann-Gibbs Blast-Wave model to fit the spectra during the extrapolation procedure. This is quantified by measuring the $\langle p_{\mathrm{T}}\rangle^{\mathrm{norm}}$ and $\langle \mathrm{d}N_{\mathrm{ch}}/\mathrm{d}\eta\rangle^{\mathrm{norm}}$ using alternative fit functions: the Lévy Tsallis [51], and Hagedorn [52] parameterizations. The maximum $\langle p_{\mathrm{T}}\rangle^{\mathrm{norm}}$ and $\langle \mathrm{d}N_{\mathrm{ch}}/\mathrm{d}\eta\rangle^{\mathrm{norm}}$ deviation with respect to the results from using the nominal fit function is assigned as the systematic uncertainty.

Finally, the total systematic uncertainty is given by the sum in quadrature of the different sources of systematic uncertainty. The dominant source of systematic uncertainty comes from the vertex and track selections. The total relative systematic uncertainty on the $\langle p_{\mathrm{T}}\rangle^{\mathrm{norm}}$ is

JHEP11(2025)076

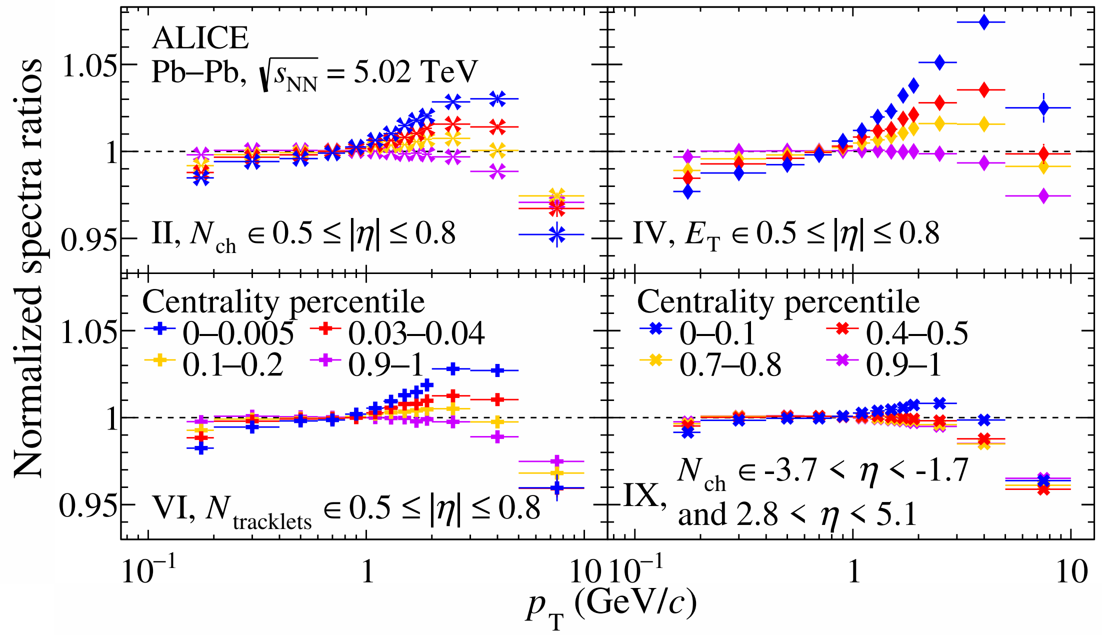

Figure 2. Normalized spectra ratios as a function of the transverse momentum in Pb-Pb collisions at $\sqrt{s_{NN}} = 5.02$ TeV. Results are shown for centrality estimators based on N_{ch} (top left), E_T (top right), $N_{tracklets}$ (bottom left) within $0.5 \leq |\eta| \leq 0.8$, and N_{ch} within $-3.7 < \eta < -1.7$ and $2.8 < \eta < 5.1$ (bottom right). Each panel displays normalized ratios for selected centrality classes. The centrality percentile legend in the bottom left panel applies to mid-rapidity estimators, while the legend in the bottom right panel applies to the forward estimator. Error bars represent statistical uncertainties. Systematic uncertainties, which are largely canceled due to their common origin in both the numerator and denominator, are not shown.

about 0.23% for the most central collisions and decreases to about 0.06% for collisions in the 4.5–5% centrality range. The total systematic uncertainty on the $\langle dN_{ch}/d\eta \rangle^{norm}$ is negligible.

4 Results and discussion

Figure 2 shows the ratios of normalized transverse-momentum spectra for the most central collisions using the following centrality estimators: $N_{tracklets}$, N_{ch}, $E_T \in 0.5 \leq |\eta| \leq 0.8$, and $N_{ch} \in -3.7 < \eta < -1.7$ and $2.8 < \eta < 5.1$. The normalized ratios are defined as

$$\frac{(d^2N/\langle dN_{ch}/d\eta \rangle d\eta dp_T)^{\text{Centrality percentile}}}{(d^2N/\langle dN_{ch}/d\eta \rangle d\eta dp_T)^{0\text{–}5\%}}\,. \tag{4.1}$$

The normalized ratios are shown for the centrality estimators with pseudorapidity gap between the region to estimate the collision centrality and the region to measure the p_T spectra. The charged-particle multiplicity based centrality estimators with the SPD and TPC detectors show a yield depletion for $p_T \lesssim 1\,\text{GeV}/c$ and a pronounced enhancement in the $1 < p_T < 6\,\text{GeV}/c$ interval with a maximum at $p_T \approx 4\,\text{GeV}/c$ for the most central collisions. This observation is reminiscent of radial flow [44, 53]. The radial-flow effects are the strongest for the most central collisions and diminish towards less central events. Furthermore, the normalized ratios in the 6–10 GeV/c transverse-momentum interval decrease,

JHEP11(2025)076

which suggests that any increase of the $\langle p_{\rm T}\rangle$ for ultracentral collisions with respect to the average transverse momentum in the reference class (0–5%) is primarily attributed to the entropy fluctuations and the hydrodynamic expansion of the QGP rather than to the effects of jet fragmentation [13, 15]. The normalized $p_{\rm T}$-spectra ratios for events selected with the V0 detector (bottom right panel in figure 2) show similar trends although the height of the radial-flow bump is considerably smaller compared to the mid-rapidity estimators. The spectra ratios with the $E_{\rm T}$-based centrality estimator (top right panel in figure 2) also show a yield depletion at low transverse momentum, however they show a sharp ratio increase above $p_{\rm T} = 1\,{\rm GeV}/c$ for the most central bin, and do not go back below 1 for $p_{\rm T} \gtrsim 5\,{\rm GeV}/c$. This observation suggests a tight short-range correlation between the activity in the centrality region and the region where the $p_{\rm T}$ spectrum is measured, leading to a $p_{\rm T}$ bias expected to give a higher $\langle p_{\rm T}\rangle$ compared with the one found using the $N_{\rm ch}$-based centrality estimators.

Measured charged-particle multiplicity distributions from central collisions are well described by a Gaussian distribution at fixed-impact parameter (b) [54]. The charged-particle density at the *knee* is denoted by $\langle {\rm d}N_{\rm ch}/{\rm d}\eta\rangle_{\rm knee}$, and it is defined as the mean value of the charged-particle density distribution for collisions with $b = 0$, while the standard deviation of this distribution is represented by $\sigma_{\rm knee}$ [54]. The mean and standard deviation at the knee are determined by fitting the $\langle {\rm d}N_{\rm ch}/{\rm d}\eta\rangle^{\rm norm}$-dependent event fraction distribution with a model for the multiplicity distribution for fixed-impact parameter. Importantly, this model does not rely on the concept of participant nucleons or any microscopic model of the collision. The $\langle {\rm d}N_{\rm ch}/{\rm d}\eta\rangle^{\rm norm}$ and $\sigma/\sigma^{0-5\%}$ at the knee are denoted by $\langle {\rm d}N_{\rm ch}/{\rm d}\eta\rangle^{\rm norm}_{\rm knee}$ and $\sigma^{\rm norm}_{\rm knee}$, respectively. The event fraction distribution, $P(\langle {\rm d}N_{\rm ch}/{\rm d}\eta\rangle^{\rm norm})$, is modeled by the integral of $P(\langle {\rm d}N_{\rm ch}/{\rm d}\eta\rangle^{\rm norm}|b)$ over all values of b, where $P(\langle {\rm d}N_{\rm ch}/{\rm d}\eta\rangle^{\rm norm}|b)$ is the probability of $\langle {\rm d}N_{\rm ch}/{\rm d}\eta\rangle^{\rm norm}$ for fixed-impact parameter given by a Gaussian distribution. Each Gaussian is characterized by the normalized mean, $\overline{\langle {\rm d}N_{\rm ch}/{\rm d}\eta\rangle^{\rm norm}}(b)$ and the normalized standard deviation, $\sigma^{\rm norm}(b)$. The employed parametric forms are $\overline{\langle {\rm d}N_{\rm ch}/{\rm d}\eta\rangle^{\rm norm}}(b) = \langle {\rm d}N_{\rm ch}/{\rm d}\eta\rangle^{\rm norm}_{\rm knee}\exp(-a_1 b - a_2 b^2 - a_3 b^3)$ and $\sigma^{\rm norm}(b) = \sigma^{\rm norm}_{\rm knee}$, where a_1, a_2, and a_3 are free parameters. Ref. [54] proposes an scenario where $\sigma^{\rm norm}(b) \propto \overline{\langle {\rm d}N_{\rm ch}/{\rm d}\eta\rangle^{\rm norm}}(b)$, which is more suitable to describe the event fraction distribution of central and semicentral collisions. Since, this study focuses on ultracentral collisions, using $\sigma^{\rm norm}(b) = \sigma^{\rm norm}_{\rm knee}$ describes well the event fraction distribution of central collisions. Figure 3 illustrates the event fraction distribution as a function of $\langle {\rm d}N_{\rm ch}/{\rm d}\eta\rangle^{\rm norm}$ derived from collisions selected with the $N_{\rm ch}$-, $E_{\rm T}$-, and V0-based centrality estimators. For mid-rapidity estimators, the region for measuring $\langle {\rm d}N_{\rm ch}/{\rm d}\eta\rangle^{\rm norm}$ completely overlaps with the region for assessing collision centrality. This means both quantities are determined within $|\eta| \leq 0.8$. In figure 3, dashed vertical lines indicate the position of $\langle {\rm d}N_{\rm ch}/{\rm d}\eta\rangle^{\rm norm}_{\rm knee}$. Table 2 provides a list of $\sigma^{\rm norm}_{\rm knee}$ and $\langle {\rm d}N_{\rm ch}/{\rm d}\eta\rangle^{\rm norm}_{\rm knee}$ values for all the studied centrality estimators. Fits to the data yielded $\chi^2/{\rm ndf}$ values equal to 1.232, 0.538, and 0.028 for the $N_{\rm ch}$-, $E_{\rm T}$-, and V0-based centrality estimators, respectively.

The speed of sound, $c_{\rm s}^2$ is extracted by fitting the $\langle p_{\rm T}\rangle^{\rm norm}$ versus $\langle {\rm d}N_{\rm ch}/{\rm d}\eta\rangle^{\rm norm}$ correlation to the parameterization proposed in ref. [13], based on the relation $\langle p_{\rm T}\rangle \propto s^{c_{\rm s}^2}$ with s representing the entropy density

$$\langle p_{\rm T}\rangle^{\rm norm} = \left(\frac{\langle {\rm d}N_{\rm ch}/{\rm d}\eta\rangle^{\rm norm}}{f(\langle {\rm d}N_{\rm ch}/{\rm d}\eta\rangle^{\rm norm}, \langle {\rm d}N_{\rm ch}/{\rm d}\eta\rangle^{\rm norm}_{\rm knee}, \sigma^{\rm norm}_{\rm knee})}\right)^{c_{\rm s}^2}, \tag{4.2}$$

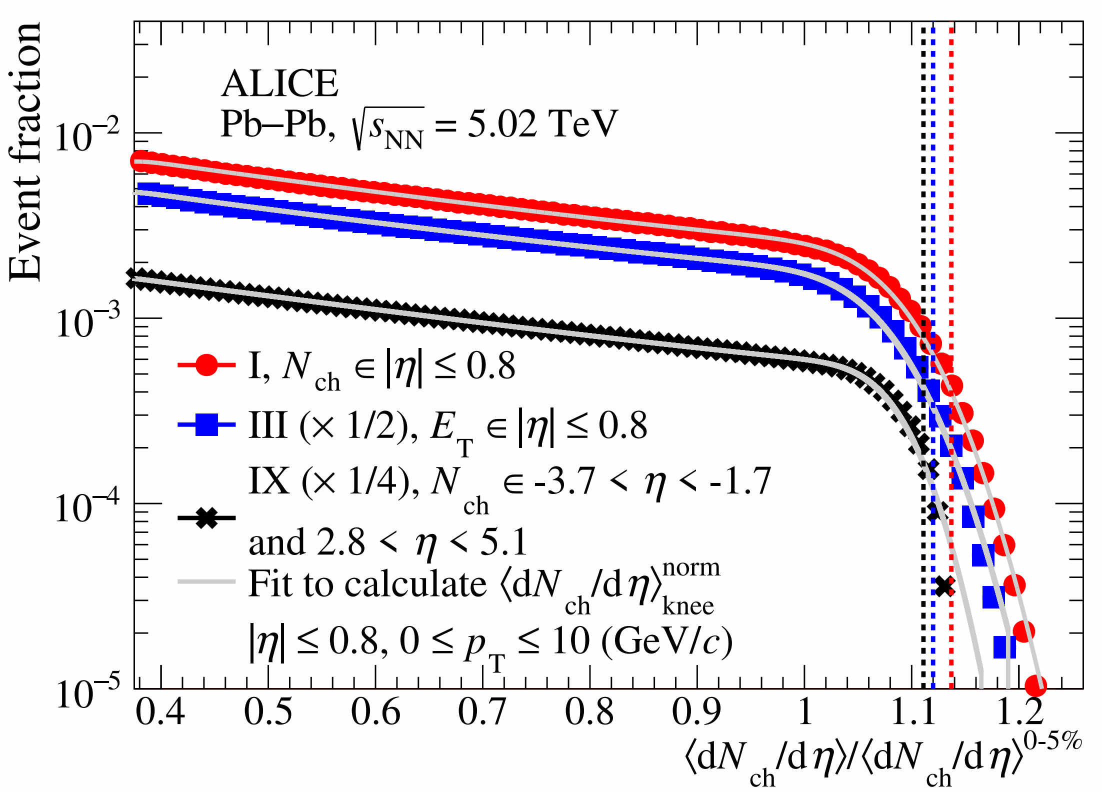

Figure 3. Event fraction distribution as a function of the normalized charged-particle density in Pb-Pb collisions at $\sqrt{s_{NN}} = 5.02$ TeV. Centrality classification is based on N_{ch} (red circles) and E_T (blue squares) in $|\eta| \leq 0.8$, and on forward N_{ch} for the V0 (black crosses). $\langle dN_{ch}/d\eta\rangle^{norm}$ is derived from the extrapolated spectra in $|\eta| \leq 0.8$. Gray curves represent fits using the model from ref. [54]. The positions of $\langle dN_{ch}/d\eta\rangle^{norm}_{knee}$, indicated by dashed vertical lines, are 1.137, 1.120, and 1.111 for the N_{ch}-, E_T-, and V0-based centrality estimators, respectively.

Label	$\langle dN_{ch}/d\eta\rangle^{norm}_{knee}$	σ^{norm}_{knee}	Speed of sound (c_s^2)
I	1.1370 ± 0.0004 (stat.)	0.0348 ± 0.0005 (stat.)	0.1369 ± 0.0007 (stat.) ± 0.0015 (syst.)
II	1.1040 ± 0.0021 (stat.)	0.0202 ± 0.0006 (stat.)	0.1795 ± 0.0018 (stat.) ± 0.0083 (syst.)
III	1.1200 ± 0.0767 (stat.)	0.0359 ± 0.0033 (stat.)	0.4374 ± 0.0006 (stat.) ± 0.0184 (syst.)
IV	1.1010 ± 0.0131 (stat.)	0.0201 ± 0.0006 (stat.)	0.3058 ± 0.0015 (stat.) ± 0.0143 (syst.)
V	1.1450 ± 0.0001 (stat.)	0.0268 ± 0.0006 (stat.)	0.1773 ± 0.0013 (stat.) ± 0.0066 (syst.)
VI	1.1090 ± 0.0006 (stat.)	0.0185 ± 0.0012 (stat.)	0.1873 ± 0.0025 (stat.) ± 0.0143 (syst.)
VII	1.1120 ± 0.0026 (stat.)	0.0183 ± 0.0023 (stat.)	0.2083 ± 0.0024 (stat.) ± 0.0249 (syst.)
VIII	1.1248 ± 0.0169 (stat.)	0.0227 ± 0.0020 (stat.)	0.1473 ± 0.0023 (stat.) ± 0.0119 (syst.)
IX	1.1144 ± 0.0024 (stat.)	0.0186 ± 0.0023 (stat.)	0.1146 ± 0.0028 (stat.) ± 0.0065 (syst.)

Table 2. Values of σ^{norm}_{knee} and $\langle dN_{ch}/d\eta\rangle^{norm}_{knee}$ obtained from fitting the event fraction distribution shown in figure 3. The fit parameters are given for all the centrality estimators. The last column lists the values of c_s^2 for all the centrality estimators in natural units. These values are obtained from a fit to the correlation between $\langle p_T\rangle^{norm}$ and $\langle dN_{ch}/d\eta\rangle^{norm}$ using eq. (4.2). The definition of each estimator is given in table 1.

with

$$f(\langle \mathrm{d}N_{\mathrm{ch}}/\mathrm{d}\eta\rangle^{\mathrm{norm}}, \langle \mathrm{d}N_{\mathrm{ch}}/\mathrm{d}\eta\rangle^{\mathrm{norm}}_{\mathrm{knee}}, \sigma^{\mathrm{norm}}_{\mathrm{knee}}) = \langle \mathrm{d}N_{\mathrm{ch}}/\mathrm{d}\eta\rangle^{\mathrm{norm}} - \sigma^{\mathrm{norm}}_{\mathrm{knee}}\sqrt{\frac{2}{\pi}}\frac{\exp\left(-\frac{(\langle \mathrm{d}N_{\mathrm{ch}}/\mathrm{d}\eta\rangle^{\mathrm{norm}} - \langle \mathrm{d}N_{\mathrm{ch}}/\mathrm{d}\eta\rangle^{\mathrm{norm}}_{\mathrm{knee}})^2}{2(\sigma^{\mathrm{norm}}_{\mathrm{knee}})^2}\right)}{\mathrm{erfc}\left(\frac{\langle \mathrm{d}N_{\mathrm{ch}}/\mathrm{d}\eta\rangle^{\mathrm{norm}} - \langle \mathrm{d}N_{\mathrm{ch}}/\mathrm{d}\eta\rangle^{\mathrm{norm}}_{\mathrm{knee}}}{\sqrt{2}\sigma^{\mathrm{norm}}_{\mathrm{knee}}}\right)}. \tag{4.3}$$

The values of $\langle \mathrm{d}N_{\mathrm{ch}}/\mathrm{d}\eta\rangle^{\mathrm{norm}}_{\mathrm{knee}}$ and $\sigma^{\mathrm{norm}}_{\mathrm{knee}}$ are fixed in eq. (4.3) using the values reported in table 2. Consequently, the function presented in eq. (4.3) depends on $\langle \mathrm{d}N_{\mathrm{ch}}/\mathrm{d}\eta\rangle^{\mathrm{norm}}$. The $f(\langle \mathrm{d}N_{\mathrm{ch}}/\mathrm{d}\eta\rangle^{\mathrm{norm}})$ has a rather simple behavior: $f(\langle \mathrm{d}N_{\mathrm{ch}}/\mathrm{d}\eta\rangle^{\mathrm{norm}}) = \langle \mathrm{d}N_{\mathrm{ch}}/\mathrm{d}\eta\rangle^{\mathrm{norm}}$ in the limit when $\langle \mathrm{d}N_{\mathrm{ch}}/\mathrm{d}\eta\rangle^{\mathrm{norm}}$ is smaller than the ratio of particle densities at the knee. Thus, eq. (4.2) becomes, $\langle p_{\mathrm{T}}\rangle^{\mathrm{norm}} = 1$ in this limit. Conversely, when $\langle \mathrm{d}N_{\mathrm{ch}}/\mathrm{d}\eta\rangle^{\mathrm{norm}}$ is larger than the ratio of particle densities at the knee, $f(\langle \mathrm{d}N_{\mathrm{ch}}/\mathrm{d}\eta\rangle^{\mathrm{norm}}) \approx \langle \mathrm{d}N_{\mathrm{ch}}/\mathrm{d}\eta\rangle^{\mathrm{norm}}_{\mathrm{knee}}$, and eq. (4.2) becomes: $\langle p_{\mathrm{T}}\rangle^{\mathrm{norm}} \propto (\langle \mathrm{d}N_{\mathrm{ch}}/\mathrm{d}\eta\rangle^{\mathrm{norm}}/\langle \mathrm{d}N_{\mathrm{ch}}/\mathrm{d}\eta\rangle^{\mathrm{norm}}_{\mathrm{knee}})^{c_{\mathrm{s}}^2}$. For example, for the V0-based centrality estimator, $f(\langle \mathrm{d}N_{\mathrm{ch}}/\mathrm{d}\eta\rangle^{\mathrm{norm}})$ is equal to 1.099 at the knee.

Table 2 presents the obtained c_{s}^2 values, along with their statistical and total systematic uncertainties, for each centrality estimator. The statistical uncertainty is calculated by independently shifting each $\langle p_{\mathrm{T}}\rangle^{\mathrm{norm}}$ data point by a fraction of its statistical uncertainty. Each fraction is randomly drawn from a standard normal distribution, and each new $\langle p_{\mathrm{T}}\rangle^{\mathrm{norm}}$ versus $\langle \mathrm{d}N_{\mathrm{ch}}/\mathrm{d}\eta\rangle^{\mathrm{norm}}$ correlations is refitted. This procedure is repeated a thousand times, resulting in a distribution of c_{s}^2 values. The c_{s}^2 distribution is then fitted with a Gaussian function, and its variance is associated with the statistical uncertainty on c_{s}^2. Two sources of systematic uncertainty are considered. The first source arises from the choice of the Boltzmann-Gibbs Blast-Wave [46] model to extrapolate the p_{T} spectra. To assess this, the c_{s}^2 is extracted using alternative models: the Lévy-Tsallis [51] and Hagedorn [52] (described in section 3). The maximum difference between c_{s}^2 values obtained using the nominal and alternative models is assigned as the systematic uncertainty. The second source stems from the imprecise measurement of $\sigma^{\mathrm{norm}}_{\mathrm{knee}}$ and $\langle \mathrm{d}N_{\mathrm{ch}}/\mathrm{d}\eta\rangle^{\mathrm{norm}}_{\mathrm{knee}}$. This is assessed by incoherently shifting these parameters around their nominal values. The shift amount is determined by their uncertainty multiplied by a random factor drawn from a Gaussian distribution with a mean of zero and standard deviation of one. Then, the $\langle p_{\mathrm{T}}\rangle^{\mathrm{norm}}$ distribution is fit for each shift. This process is repeated a thousand times, generating a distribution of c_{s}^2 values. The standard deviation of this distribution, fitted with a Gaussian function, is assigned as the systematic uncertainty due to the imprecise measurement of knee parameters. The total systematic uncertainty on the value of c_{s}^2 is obtained by summing in quadrature the systematic uncertainties from model dependence and knee parameter uncertainty.

Figure 4 shows the $\langle p_{\mathrm{T}}\rangle^{\mathrm{norm}}$ as a function of $\langle \mathrm{d}N_{\mathrm{ch}}/\mathrm{d}\eta\rangle^{\mathrm{norm}}$ for the different centrality estimators with fits to the data using eq. (4.2). The top left panel shows the results with pseudorapidity gap: centrality estimated in $0.5 \leq |\eta| < 0.8$, and $\langle p_{\mathrm{T}}\rangle$ and $\langle \mathrm{d}N_{\mathrm{ch}}/\mathrm{d}\eta\rangle$ measured in $|\eta| \leq 0.3$. The event activity is quantified using N_{ch} and $N_{\mathrm{tracklets}}$ in the TPC and SPD detectors, respectively. Both centrality estimators give similar results suggesting that the yield of particles with transverse momentum below $p_{\mathrm{T}} = 0.15\,\mathrm{GeV}/c$ has a negligible impact on

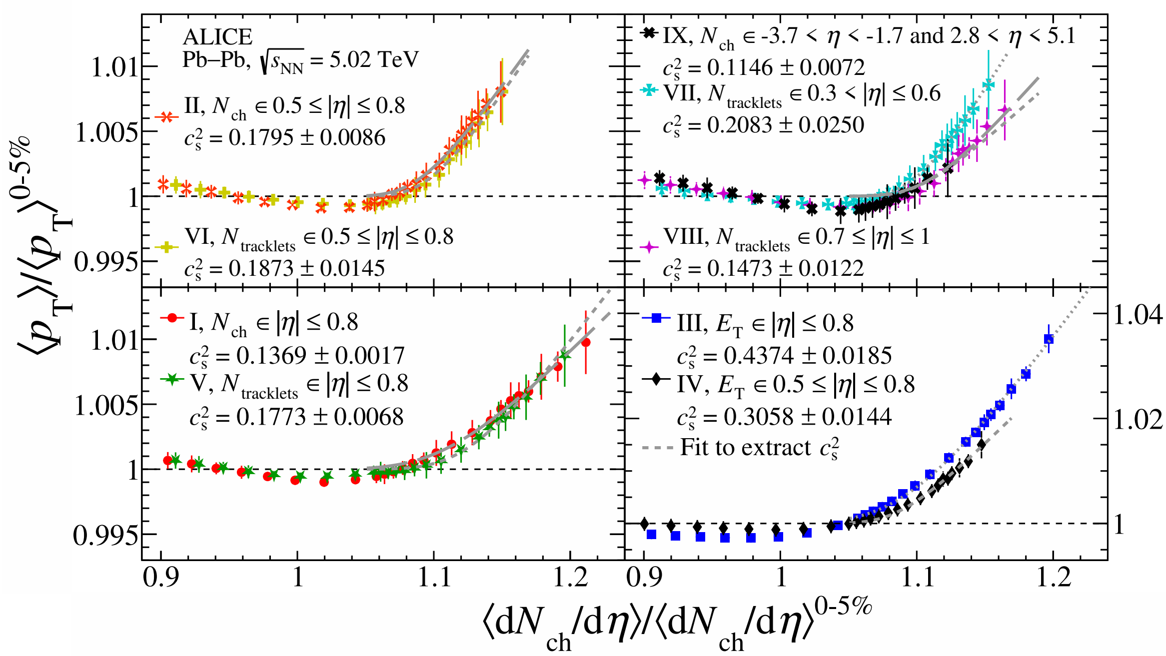

Figure 4. Correlation between $\langle p_{\rm T}\rangle^{\rm norm}$ and $\langle {\rm d}N_{\rm ch}/{\rm d}\eta\rangle^{\rm norm}$ in Pb-Pb collisions at $\sqrt{s_{\rm NN}} = 5.02$ TeV. Each panel shows the results for different centrality estimators defined in table 1. $\langle p_{\rm T}\rangle^{\rm norm}$ and $\langle {\rm d}N_{\rm ch}/{\rm d}\eta\rangle^{\rm norm}$ are derived from the $p_{\rm T}$ spectra within the 0–10 GeV/c interval for all centrality estimators. For $E_{\rm T}$-based centrality estimators, the y-axis scale should be read from the axis located to the right of the bottom right panel. Lines on top of the data represent fits using eq. (4.2). The fit range spans from 1 to the last point. Each panel displays the corresponding c_s^2 values with their total uncertainty, determined by summing the statistical and systematic uncertainties in quadrature. Vertical uncertainty bars in each point represent the combined statistical and systematic uncertainty. The total uncertainty in the $\langle {\rm d}N_{\rm ch}/{\rm d}\eta\rangle^{\rm norm}$ is negligible and therefore not visible.

selecting collisions with similar entropy densities when using these two centrality estimators. This is further supported by the similar c_s^2 values obtained with both estimators: c_s^2 is equal to 0.1873 ± 0.0145 and 0.1795 ± 0.0086 for the SPD and TPC centrality estimators, respectively.

The top right panel of figure 4 presents the results obtained with varying pseudorapidity gaps (0, 0.4, and 0.9 units). $\langle p_{\rm T}\rangle^{\rm norm}$ with zero gap rises at a steeper rate compared to the cases with a gap, while $\langle {\rm d}N_{\rm ch}/{\rm d}\eta\rangle^{\rm norm}$ remains relatively constant regardless of the presence of the pseudorapidity gap. This can be attributed to the finite width of jets, whose fragmentation products can extend into the pseudorapidity region where $\langle p_{\rm T}\rangle$ is measured. The rise rate of $\langle p_{\rm T}\rangle^{\rm norm}$ is seen to decrease with increasing pseudorapidity gap, yielding c_s^2 values of 0.2083 ± 0.0250 (no gap), 0.1873 ± 0.0145 (gap of 0.2 units) and 0.1473 ± 0.0122 (gap of 0.4 units), for the three cases using the $N_{\rm tracklets}$ centrality estimator. While it would be interesting to investigate larger pseudorapidity gaps with the SPD detector, the strong dependence of cluster reconstruction efficiency on the primary-vertex position along the beam axis limits the maximum achievable pseudorapidity selection to one unit. The maximum pseudorapidity gap is achieved using the V0 detector. The V0 amplitude-based centrality estimator exhibits a narrower range in $\langle {\rm d}N_{\rm ch}/{\rm d}\eta\rangle^{\rm norm}$, reaching only up to 1.1, compared to the particle density obtained with SPD and TPC centrality estimators. It is known that the

JHEP11(2025)076

V0 detector has a better centrality resolution than central-barrel detectors [38]. $\langle p_{\rm T}\rangle^{\rm norm}$ with the V0 centrality estimator also increases, albeit at a lower rate, yielding the lowest speed of sound, $c_{\rm s}^2 = 0.1146 \pm 0.0072$. Accordingly, the data suggest a decreasing trend in the extracted $c_{\rm s}^2$ with increasing pseudorapidity gap width.

The bottom left panel of figure 4 shows $\langle p_{\rm T}\rangle^{\rm norm}$ using multiplicity-based centrality estimators ($N_{\rm ch}$ in the TPC and $N_{\rm tracklets}$ in the SPD). In this case, there is no pseudorapidity gap, and the pseudorapidity regions for centrality estimation and transverse-momentum spectra measurement fully overlap ($|\eta| \leq 0.8$). The $\langle {\rm d}N_{\rm ch}/{\rm d}\eta\rangle^{\rm norm}$ reach with the $N_{\rm ch}$ estimator is the highest among all centrality estimators. This is attributed to the fact that the same particles are used for both centrality determination and $p_{\rm T}$ spectra measurement within the same pseudorapidity region. Using overlapping pseudorapidity intervals introduces a multiplicity bias. Local fluctuations combined with this bias, including measurement uncertainties, lead to a broader distribution along the $\langle {\rm d}N_{\rm ch}/{\rm d}\eta\rangle^{\rm norm}$ axis, while $\langle p_{\rm T}\rangle^{\rm norm}$ remains relatively unchanged, resulting in a lower extracted $c_{\rm s}^2$ (0.1369 ± 0.0017 compared to 0.1795 ± 0.0086 with a pseudorapidity gap of 0.2 units). The $\langle p_{\rm T}\rangle^{\rm norm}$ distribution obtained using the $N_{\rm tracklets}$-based centrality estimator with full overlap also appears to be stretched along the $\langle {\rm d}N_{\rm ch}/{\rm d}\eta\rangle^{\rm norm}$ axis compared to the cases with pseudorapidity gap. This results in a steeper $\langle p_{\rm T}\rangle^{\rm norm}$ and a larger extracted $c_{\rm s}^2$ compared to the $N_{\rm ch}$ estimator. These results can be partially explained by the overlap between SPD tracklets and global tracks, causing a significant multiplicity bias but still smaller than the one introduced by estimating both centrality and $\langle {\rm d}N_{\rm ch}/{\rm d}\eta\rangle^{\rm norm}$ using the same pool of global tracks.

The bottom right panel of figure 4 shows the results obtained using the transverse energy-based centrality estimators. The centrality estimator with full pseudorapidity overlap ($|\eta| \leq 0.8$) introduces a transverse-momentum bias leading to the largest $\langle p_{\rm T}\rangle^{\rm norm}$. Furthermore, the $\langle {\rm d}N_{\rm ch}/{\rm d}\eta\rangle^{\rm norm}$ reaches 1.18, suggesting an additional multiplicity bias due to jet fragmentation. Introducing a 0.2 unit pseudorapidity gap reduces $\langle {\rm d}N_{\rm ch}/{\rm d}\eta\rangle^{\rm norm}$ to around 1.14, consistent with the values obtained using SPD and TPC multiplicity-based estimators with the same gap. Moreover, the $\langle p_{\rm T}\rangle^{\rm norm}$ rise becomes less steep compared to the case with full overlap, although the extracted $c_{\rm s}^2$ is higher than that obtained with multiplicity-based estimators. This could be attributed to an interplay between the finite width of jets and the transverse-momentum bias. Finally, the different $\langle p_{\rm T}\rangle^{\rm norm}$ distributions measured using the multiplicity-based centrality estimators exhibit a shallow local minimum at $\langle {\rm d}N_{\rm ch}/{\rm d}\eta\rangle^{\rm norm} \approx 1.04$. This feature is less noticeable when the $E_{\rm T}$-based centrality estimator is employed. The minimum corresponds to collisions in the 0.9–1% centrality range. In ref. [14], it is discussed that while the average entropy density, average temperature at hydrodynamic initialization, QGP size, and impact parameter all vary monotonically near 1% centrality, the impact parameter essentially stops changing below 1% centrality. This observation is consistent with the observed centrality percentile at which the plateau in the $\langle N_{\rm part}\rangle$ distribution commences (see figure 1). Therefore, the local minimum could be attributed to the impact parameter ceasing to vary, or varying only minimally.

Appendix A shows the correlation between $\langle p_{\rm T}\rangle^{\rm norm}$ and $\langle {\rm d}N_{\rm ch}/{\rm d}\eta\rangle^{\rm norm}$ using the $E_{\rm T}$-based and $N_{\rm ch}$-based centrality estimators. In both cases, a minimum pseudorapidity gap of 0.2 units was maintained between the pseudorapidity region used for centrality estimation and the region used to measure $\langle p_{\rm T}\rangle^{\rm norm}$ and $\langle {\rm d}N_{\rm ch}/{\rm d}\eta\rangle^{\rm norm}$. The $E_{\rm T}$-based centrality estimator

JHEP11(2025)076

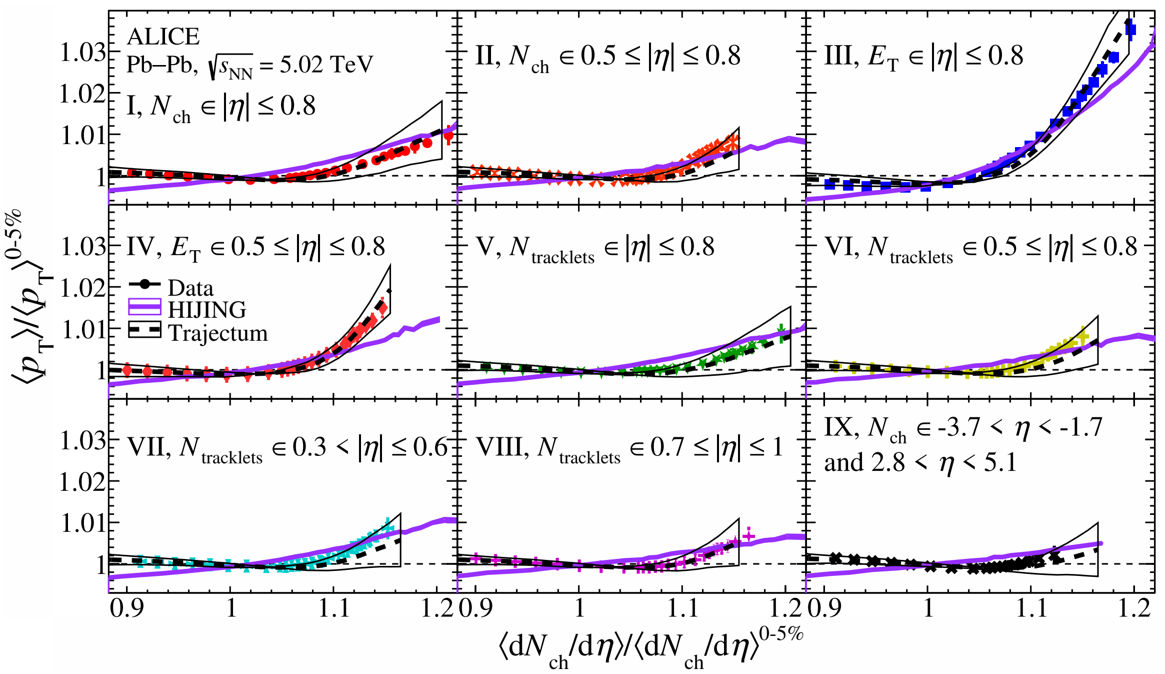

Figure 5. Correlation between $\langle p_T \rangle^{norm}$ and $\langle dN_{ch}/d\eta \rangle^{norm}$ in Pb-Pb collisions at $\sqrt{s_{NN}} = 5.02$ TeV. Each panel shows the results for different centrality estimators defined in table 1. The data are compared with predictions from the HIJING [42] and Trajectum [55–57] models, represented by continuous and dashed lines, respectively. The bands around the Trajectum predictions represent the sum in quadrature of the statistical and systematic uncertainties, with the latter being the dominant source. For the HIJING predictions, only the statistical uncertainty is shown (not visible in the plot).

uses charged particles with a lower p_T threshold of 0.15 GeV/c, while the N_{ch}-based centrality estimator uses a lower p_T threshold of 0.45 GeV/c. This selection is motivated by a prediction from the Trajectum model [55–57]: defining an N_{ch}-based centrality estimator using charged particles with a relatively high p_T threshold selects collisions with a higher $\langle p_T \rangle^{norm}$, compared to using a lower p_T threshold. A fit to the $\langle p_T \rangle^{norm}$ versus $\langle dN_{ch}/d\eta \rangle^{norm}$ correlation with the N_{ch}-based centrality estimator and with a minimum pseudorapidity gap of 0.2 units yields an extracted c_s^2 value that is about 27% higher when the lower p_T threshold is set to 0.45 GeV/c compared to the value obtained using $N_{tracklets}$ for centrality estimation with a lower p_T threshold of 0.03 GeV/c and with the same pseudorapidity gap. Furthermore, it is shown that the extraction of the c_s^2 is robust against variations in the fit range.

Figure 5 shows the $\langle p_T \rangle^{norm}$ versus $\langle dN_{ch}/d\eta \rangle^{norm}$ correlation in data compared to predictions by the HIJING [42] and Trajectum [55–57] models for the different centrality estimators defined in table 1. The HIJING model implements an independent source particle production picture, where each collision is modeled as a superposition of independent nucleon-nucleon collisions, neglecting interactions between the sources. Trajectum incorporates a generalized T$_R$ENTo [58] initial stage, followed by a viscous hydrodynamic stage and hadronization using SMASH [59]. It utilizes a continuous hybrid equation of state (EoS) that interpolates between the hadron resonance gas (HRG) at low temperatures and the lattice result by HotQCD at high temperatures [17]. Samples of ultracentral collisions are simulated using different EoS parameter settings [14]. The dashed lines in figure 5 represent the average Trajectum predictions, with the bands indicating the sum in quadrature of the statistical and systematic uncertainties. The latter are given by the one-standard-deviation uncertainty due to variations in EoS parameters. Trajectum predictions for $\langle p_{\mathrm{T}}\rangle^{\mathrm{norm}}$ versus $\langle \mathrm{d}N_{\mathrm{ch}}/\mathrm{d}\eta\rangle^{\mathrm{norm}}$ are in good agreement with the data, reproducing the minimum and the subsequent rise in $\langle p_{\mathrm{T}}\rangle^{\mathrm{norm}}$ and capturing the experimental biases of all centrality estimators, in particular the rapid rise of $\langle p_{\mathrm{T}}\rangle^{\mathrm{norm}}$ observed with the E_{T}-based estimator. HIJING predicts a steady increase in $\langle p_{\mathrm{T}}\rangle^{\mathrm{norm}}$ with increasing $\langle \mathrm{d}N_{\mathrm{ch}}/\mathrm{d}\eta\rangle^{\mathrm{norm}}$ for all centrality estimators, with a steeper rise with the E_{T}-based estimator with no pseudorapidity gap (less pronounced using the same estimator with a gap of 0.2 units). In the ultracentral-collision limit the E_{T}-based estimator clearly favors events with an enhanced production of multiple jets [42], leading to a larger $\langle p_{\mathrm{T}}\rangle^{\mathrm{norm}}$. Since HIJING does not include QGP formation, its reproduction of the observed selection biases suggests that the rise of the $\langle p_{\mathrm{T}}\rangle$ in ultracentral collisions may not directly probe entropy fluctuations in the QGP.

Figure 6 illustrates the dependence of the extracted c_{s}^2 on the pseudorapidity gap between the centrality determination region and the transverse-momentum spectra measurement region. The highest c_{s}^2 value is observed with the transverse energy-based centrality estimation and full pseudorapidity overlap. This configuration biases $\langle p_{\mathrm{T}}\rangle^{\mathrm{norm}}$, potentially introducing a jet-fragmentation bias. Introducing a pseudorapidity gap in the transverse-energy centrality estimation reduces both $\langle p_{\mathrm{T}}\rangle^{\mathrm{norm}}$ and $\langle \mathrm{d}N_{\mathrm{ch}}/\mathrm{d}\eta\rangle^{\mathrm{norm}}$, leading to a lower c_{s}^2 of approximately 0.3. However, this value remains significantly higher than those obtained with multiplicity-based estimators, likely due to the contribution of intermediate-to-high p_{T} particles from jet fragmentation to the spectra. Notably, the multiplicity-based centrality estimator with the SPD and full overlap yields a c_{s}^2 (0.1773 ± 0.0068) similar to that obtained with a larger pseudorapidity gap (0.1873 ± 0.0145). This similarity arises from a multiplicity bias in the no-gap case, which stretches the $\langle p_{\mathrm{T}}\rangle^{\mathrm{norm}}$ versus $\langle \mathrm{d}N_{\mathrm{ch}}/\mathrm{d}\eta\rangle^{\mathrm{norm}}$ distribution along the $\langle \mathrm{d}N_{\mathrm{ch}}/\mathrm{d}\eta\rangle^{\mathrm{norm}}$ axis, resulting in a lower extracted c_{s}^2. When the centrality and the p_{T} spectrum are determined in non-overlapping regions, the c_{s}^2 found with the $N_{\mathrm{tracklets}}$ centrality estimator decreases with increasing pseudorapidity gap. This dependence on the pseudorapidity gap is further supported by the even lower c_{s}^2 values obtained with the V0 centrality estimator.

Figure 6 also presents the extracted c_{s}^2 value by the CMS collaboration [21], where the centrality is determined in the forward rapidity region $(3 \leq |\eta| \leq 5)$ using the top 0–5% most energetic events. The $\langle p_{\mathrm{T}}\rangle^{\mathrm{norm}}$ versus $\langle \mathrm{d}N_{\mathrm{ch}}/\mathrm{d}\eta\rangle^{\mathrm{norm}}$ correlation is measured in $|\eta| < 0.5$. CMS reports a $c_{\mathrm{s}}^2 = 0.241 \pm 0.002$ (stat.) $\pm$ 0.016 (syst.) in natural units, consistent with Lattice QCD expectations. This value falls between the c_{s}^2 values obtained using the charged-particle multiplicity and transverse-energy centrality estimators in ALICE data. The CMS experimental setup employs a significantly wider pseudorapidity gap between the centrality and observable pseudorapidity regions compared to ALICE, effectively suppressing short-range $\langle p_{\mathrm{T}}\rangle$–$\langle p_{\mathrm{T}}\rangle$ correlations due to jet finite width. However, even with this gap, the E_{T}-based centrality estimator remains sensitive to long-range $\langle p_{\mathrm{T}}\rangle$–$\langle p_{\mathrm{T}}\rangle$ correlations [60].

Figure 6 shows the extracted c_{s}^2 values using simulated events from the Trajectum [55–57] and HIJING [42] models. The model values are extracted by fitting the predicted $\langle p_{\mathrm{T}}\rangle^{\mathrm{norm}}$ versus $\langle \mathrm{d}N_{\mathrm{ch}}/\mathrm{d}\eta\rangle^{\mathrm{norm}}$ correlation using the same procedure and centrality estimators as for

JHEP11(2025)076

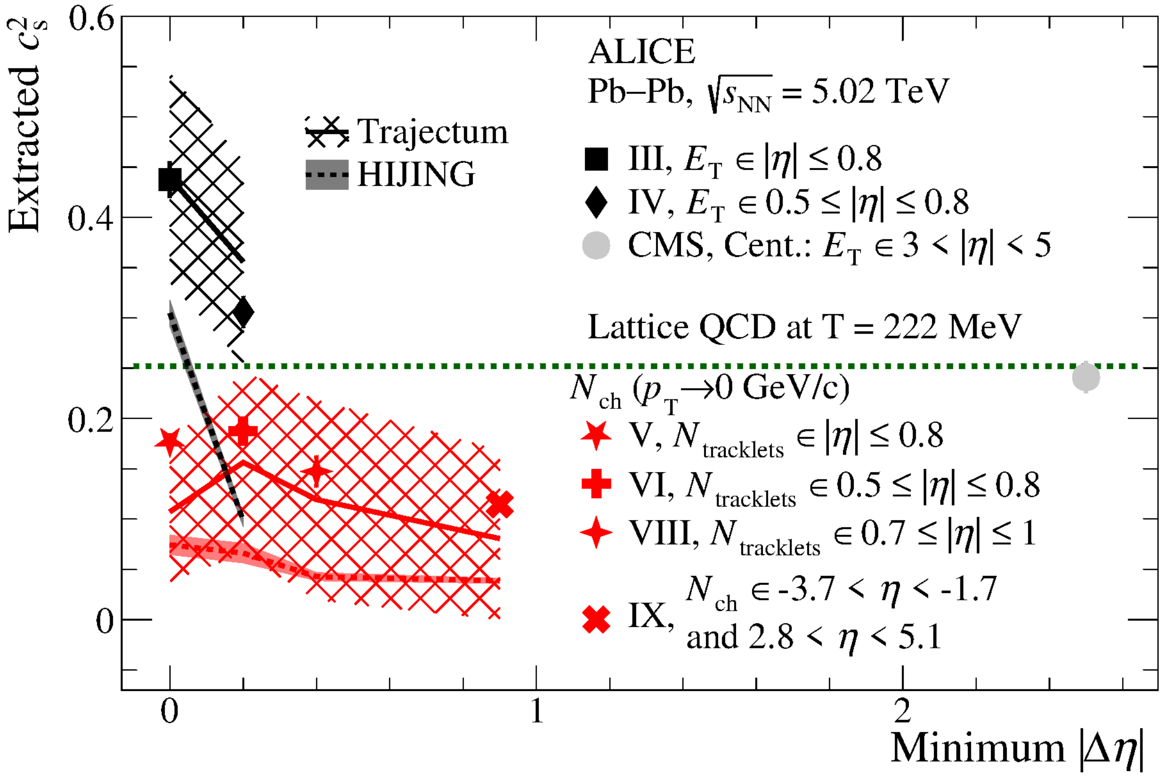

Figure 6. Extracted c_s^2 as a function of the minimum pseudorapidity gap between the centrality estimation and transverse-momentum spectra measurement in Pb-Pb collisions at $\sqrt{s_{NN}} = 5.02$ TeV. The results are compared with the c_s^2 value measured by the CMS collaboration (with a minimum $|\Delta\eta| = 2.5$) [21]. The uncertainty bars around the data points represent the sum in quadrature of the statistical and systematic uncertainties (not visible). Predictions from Trajectum [55–57] are shown as continuous lines, with mesh bands indicating the total uncertainty (statistical and systematic combined in quadrature). Predictions from the HIJING [42] model are shown as dashed lines, with shaded bands representing statistical uncertainty only. See the main text for details on the uncertainty estimation in the model c_s^2 values. The horizontal dashed green line indicates the Lattice QCD prediction of c_s^2 for deconfined matter, as calculated by the HotQCD collaboration [17]. Centrality-estimator definitions are presented in table 1.

the data. The uncertainty in the Trajectum c_s^2 values is estimated by shifting the $\langle p_T \rangle^{norm}$ distribution between its minimum and maximum bounds, as determined by its point-by-point systematic uncertainty, and then refitting. The difference between the minimum and maximum extracted c_s^2 values, relative to the nominal value, is assigned as the systematic uncertainty. Only the statistical uncertainty is considered for the HIJING predictions. Trajectum predictions are consistent with the data within 15% for the E_T-based centrality estimator, but exhibit increasing deviation with increasing pseudorapidity gap for multiplicity-based centrality estimators. In contrast, the HIJING c_s^2 values are systematically lower than the data, indicating that hydrodynamic evolution is essential for a quantitative description.

Figure 7 presents the self-normalized higher-order moments of $[p_T]$ as a function of $\langle dN_{ch}/d\eta \rangle^{norm}$. The left column displays results from the charged-particle centrality estimator at mid-rapidity, while the right column shows those from the transverse-energy centrality

JHEP11(2025)076

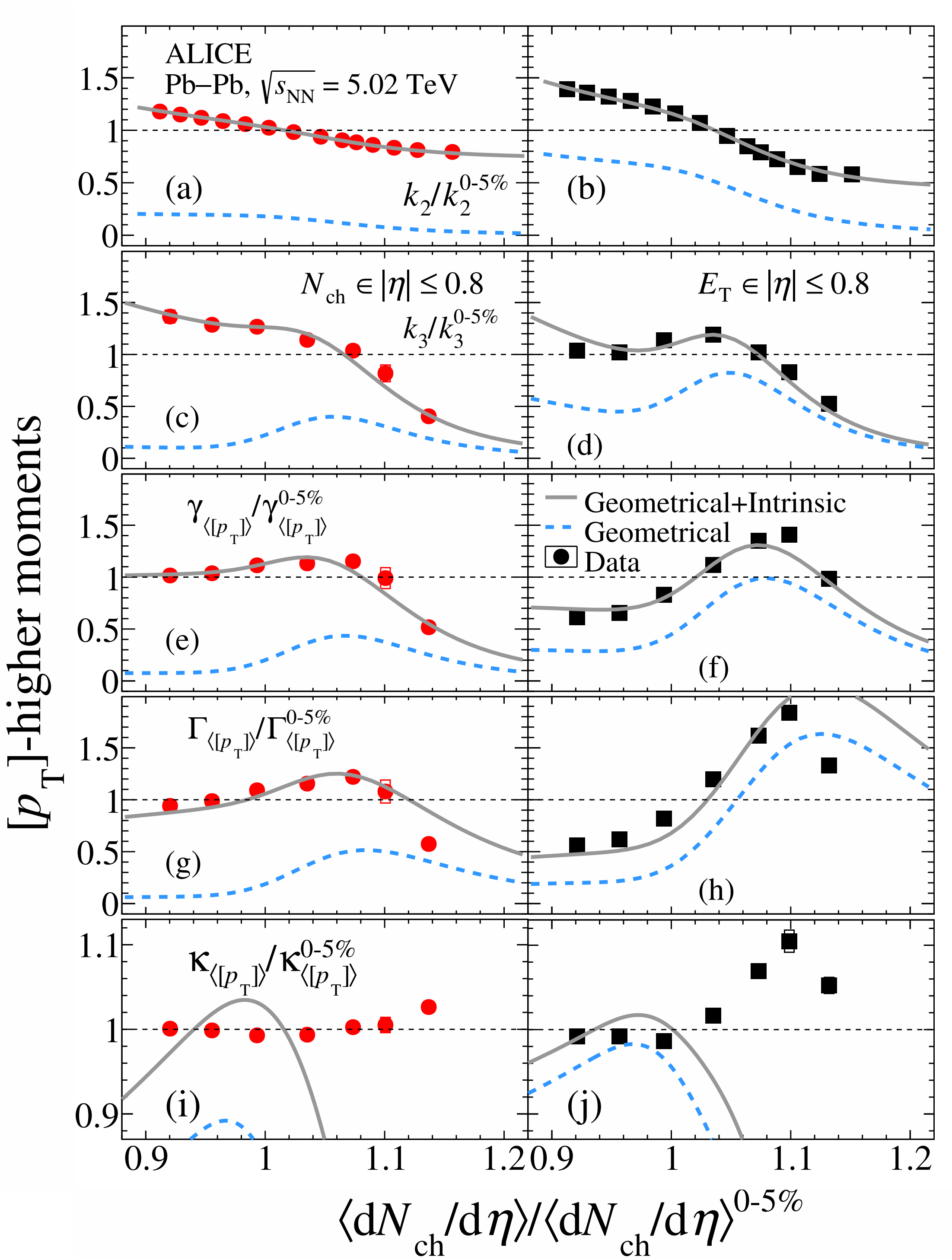

Figure 7. Higher-order moments of $[p_T]$ measured for events selected with the N_{ch} (I) and E_T (III) centrality estimators at mid-rapidity in Pb-Pb collisions at $\sqrt{s_{NN}} = 5.02\,\text{TeV}$ are shown in the left and right columns, respectively. The k_2^{norm} distributions are fitted with a two-component model (continuous gray line), where the estimated Geometrical component is also shown (dotted-dashed blue line) [27]. The curves for the k_3^{norm}, $\gamma^{norm}_{\langle[p_T]\rangle}$, $\Gamma^{norm}_{\langle[p_T]\rangle}$, and $\kappa^{norm}_{\langle[p_T]\rangle}$ distributions correspond to predictions based on the fit of k_2^{norm} [26].

estimator. Results using the V0M centrality estimator are similar to those from the mid-rapidity multiplicity-based centrality estimator and are shown in appendix B.

Under the assumption of independent nucleon-nucleon particle production, higher-order moments of $[p_{\mathrm{T}}]$ are expected to depend on collision centrality and system size, as characterized by N_{part}. The n^{th}-order cumulant is expected to scale as $\propto 1/N_{\mathrm{part}}^{(n-1)}$, or equivalently as $\propto 1/N_{\mathrm{ch}}^{(n-1)}$ [61, 62]. Consequently, $k_2^{\mathrm{norm}} \propto 1/N_{\mathrm{part}}$. The k_2^{norm} distributions in panels (a) and (b) exhibit a decreasing trend with increasing $\langle \mathrm{d}N_{\mathrm{ch}}/\mathrm{d}\eta\rangle^{\mathrm{norm}}$. While the k_2^{norm} decreases proportionally to $1/\langle \mathrm{d}N_{\mathrm{ch}}/\mathrm{d}\eta\rangle^{\mathrm{norm}}$ with the N_{ch}-based centrality estimator, the decrease is more rapid with the E_{T}-based estimator for $\langle \mathrm{d}N_{\mathrm{ch}}/\mathrm{d}\eta\rangle^{\mathrm{norm}} \lesssim 1.1$. The non-trivial evolution of k_2^{norm} with the E_{T} estimator can be attributed to the interplay of two effects: jet-fragmentation bias, arising from the overlap of centrality assessment and k_2^{norm} measurement within the same pseudorapidity window, and volume fluctuations, stemming from the centrality-dependent $\langle N_{\mathrm{part}}\rangle$ (see figure 1). The E_{T} estimator selects collisions with lower $\langle N_{\mathrm{part}}\rangle$ compared to the N_{ch} estimator, resulting in larger volume fluctuations.

For a fixed $\langle \mathrm{d}N_{\mathrm{ch}}/\mathrm{d}\eta\rangle$, the fluctuations of $[p_{\mathrm{T}}]$, quantified by its variance, $Var([p_{\mathrm{T}}]|\langle \mathrm{d}N_{\mathrm{ch}}/\mathrm{d}\eta\rangle)$, arise from both volume and quantum fluctuations. Volume fluctuations originate from impact parameter variations and are referred to as Geometrical fluctuations. Additionally, $[p_{\mathrm{T}}]$ can fluctuate even when both $\langle \mathrm{d}N_{\mathrm{ch}}/\mathrm{d}\eta\rangle$ and b are constant, these are referred to as Intrinsic fluctuations. The total variance can be expressed as $Var([p_{\mathrm{T}}]|\langle \mathrm{d}N_{\mathrm{ch}}/\mathrm{d}\eta\rangle) = (\langle \overline{[p_{\mathrm{T}}]}^2\rangle_b - \langle \overline{[p_{\mathrm{T}}]}\rangle_b^2) + \langle Var([p_{\mathrm{T}}]|\langle \mathrm{d}N_{\mathrm{ch}}/\mathrm{d}\eta\rangle)\rangle_b$, where $\overline{[p_{\mathrm{T}}]}$ represents the expected value of $[p_{\mathrm{T}}]$ as a function of b and $\langle \mathrm{d}N_{\mathrm{ch}}/\mathrm{d}\eta\rangle$, and $\langle\cdots\rangle$ denotes an average over b. The first term describes Geometrical fluctuations, while the second term represents the Intrinsic ones [27].

To fit the k_2^{norm} distribution using the two-component model described above, it is assumed that the joint probability of $\langle \mathrm{d}N_{\mathrm{ch}}/\mathrm{d}\eta\rangle^{\mathrm{norm}}$ and $[p_{\mathrm{T}}]^{\mathrm{norm}}$ at fixed-impact parameter is given by a two-dimensional Gaussian [27] distribution. This distribution is defined by five parameters: the mean and variance of $[p_{\mathrm{T}}]^{\mathrm{norm}}$ and $\langle \mathrm{d}N_{\mathrm{ch}}/\mathrm{d}\eta\rangle^{\mathrm{norm}}$, denoted by $\overline{[p_{\mathrm{T}}]^{\mathrm{norm}}}(b)$, $\overline{\langle \mathrm{d}N_{\mathrm{ch}}/\mathrm{d}\eta\rangle^{\mathrm{norm}}}(b)$, $Var([p_{\mathrm{T}}]^{\mathrm{norm}}|b)$, $Var(\langle \mathrm{d}N_{\mathrm{ch}}/\mathrm{d}\eta\rangle^{\mathrm{norm}}|b)$, and the correlation coefficient, $r(b)$, between $[p_{\mathrm{T}}]^{\mathrm{norm}}$ and $\langle \mathrm{d}N_{\mathrm{ch}}/\mathrm{d}\eta\rangle^{\mathrm{norm}}$. The $\overline{\langle \mathrm{d}N_{\mathrm{ch}}/\mathrm{d}\eta\rangle^{\mathrm{norm}}}(b)$ and $Var(\langle \mathrm{d}N_{\mathrm{ch}}/\mathrm{d}\eta\rangle^{\mathrm{norm}}|b)$, or equivalently, $\sigma^{\mathrm{norm}}(b)$, are obtained from fitting the event fraction distribution as a function of $\langle \mathrm{d}N_{\mathrm{ch}}/\mathrm{d}\eta\rangle^{\mathrm{norm}}$, as described earlier (see figure 3). Since the event-average transverse momentum is independent of collision centrality for the 30% most central collisions [63], $\overline{[p_{\mathrm{T}}]^{\mathrm{norm}}}(b)$ is assumed to be independent of b and is denoted by $\overline{[p_{\mathrm{T}}]^{\mathrm{norm}}}_0$. The variance of $[p_{\mathrm{T}}]^{\mathrm{norm}}$ for fixed b is given by $Var([p_{\mathrm{T}}]^{\mathrm{norm}}|b) = (1-r(b)^2)\sigma^2_{[p_{\mathrm{T}}]}(\langle \mathrm{d}N_{\mathrm{ch}}/\mathrm{d}\eta\rangle^{\mathrm{norm}}_{\mathrm{knee}}/\overline{\langle \mathrm{d}N_{\mathrm{ch}}/\mathrm{d}\eta\rangle^{\mathrm{norm}}}(b))^{\alpha}$, where $\sigma_{[p_{\mathrm{T}}]}$ is the standard deviation of $[p_{\mathrm{T}}]^{\mathrm{norm}}$ for collisions at zero-impact parameter, and α describes the decrease of the variance as a function of impact parameter. The parameters $\sigma_{[p_{\mathrm{T}}]}$, α, and the correlation coefficient are treated as fit parameters and are assumed to be independent of the impact parameter.

Fits to the k_2^{norm} distributions are performed separately for the N_{ch}- and E_{T}-based centrality estimators. The obtained values with the N_{ch} estimator are: $\sigma_{[p_{\mathrm{T}}]} = 4.780$, $\alpha = 1.613$, and $r = 0.921$, while for the E_{T}-based centrality estimator they are: $\sigma_{[p_{\mathrm{T}}]} = 14.539$, $\alpha = 2.512$, and $r = 0.985$. The most significant difference between the two sets of parameters is observed for $\sigma_{[p_{\mathrm{T}}]}$, which is about three times larger for the E_{T}-based centrality estimator than for the N_{ch}-based estimator. Fits to the data suggest that the E_{T}-based centrality estimator preferentially selects events where $[p_{\mathrm{T}}]$ fluctuations primarily originate from Geometrical fluctuations. The relative contribution of the Geometrical component to $[p_{\mathrm{T}}]$ fluctuations decreases from 18% (55%) at $\langle \mathrm{d}N_{\mathrm{ch}}/\mathrm{d}\eta\rangle^{\mathrm{norm}} \approx 1$ to approximately 6% (24%) at $\langle \mathrm{d}N_{\mathrm{ch}}/\mathrm{d}\eta\rangle^{\mathrm{norm}} \approx 1.14$ for the N_{ch}-(E_{T}-)based centrality estimators. In contrast, the model suggests that $[p_{\mathrm{T}}]$ variations primarily originate from Intrinsic fluctuations when using the N_{ch}-based centrality estimator. However, in the ultracentral-collision limit, the variance decreases dramatically, which can be explained by a significant suppression of the Geometrical component in this regime.

The ATLAS collaboration has reported higher-order moments of $[p_{\mathrm{T}}]$ in ultracentral collisions selected using the forward ΣE_{T} [22]. The ATLAS results exhibit closer qualitative agreement with those obtained in this study for the E_{T}-based centrality estimator, further supporting the dominance of the Geometrical component.

Panels (c) to (h) of figure 7 show the k_3^{norm} ((c) and (d)), $\gamma_{\langle[p_{\mathrm{T}}]\rangle}^{\mathrm{norm}}$ ((e) and (f)), and $\Gamma_{\langle[p_{\mathrm{T}}]\rangle}^{\mathrm{norm}}$ ((g) and (h)). Under the assumption of independent nucleon-nucleon particle production, k_3^{norm} is expected to scale as $k_3^{\mathrm{norm}} \propto 1/N_{\mathrm{part}}^2$ and $\gamma_{\langle[p_{\mathrm{T}}]\rangle}^{\mathrm{norm}} \propto 1/\sqrt{N_{\mathrm{part}}}$, while the centrality dependence of $\Gamma_{\langle[p_{\mathrm{T}}]\rangle}^{\mathrm{norm}}$ is expected to be milder than for $\gamma_{\langle[p_{\mathrm{T}}]\rangle}^{\mathrm{norm}}$ [61].

Skewness (k_3^{norm}) and kurtosis encode the non-Gaussian properties of the event-by-event $[p_{\mathrm{T}}]$ distribution. With the N_{ch}-based centrality estimator, k_3^{norm} decreases with increasing centrality, while a slight increase is observed around $\langle \mathrm{d}N_{\mathrm{ch}}/\mathrm{d}\eta\rangle^{\mathrm{norm}} \approx 1.04$. The standardized ($\gamma_{\langle[p_{\mathrm{T}}]\rangle}^{\mathrm{norm}}$) and intensive ($\Gamma_{\langle[p_{\mathrm{T}}]\rangle}^{\mathrm{norm}}$) skewness distributions exhibit an increase with $\langle \mathrm{d}N_{\mathrm{ch}}/\mathrm{d}\eta\rangle^{\mathrm{norm}}$, reaching a maximum around the knee region, followed by a decreasing trend towards the ultracentral-collision limit. The results with the E_{T}-based centrality estimator exhibit similar features, but with more pronounced maxima. The observed $\langle \mathrm{d}N_{\mathrm{ch}}/\mathrm{d}\eta\rangle^{\mathrm{norm}}$ dependence deviates from the expectations under the assumption of independent particle sources. The model predictions, overlaid on the distributions, demonstrate a dependence on the centrality estimator. The model accurately predicts the observed increase and the maximum in the standardized and intensive skewness distributions, except for the intensive skewness with the E_{T}-based centrality estimator.

Panels (i) and (j) of figure 7 show the kurtosis ($\kappa_{\langle[p_{\mathrm{T}}]\rangle}^{\mathrm{norm}}$) of the event-by-event $[p_{\mathrm{T}}]$ distribution for N_{ch} and E_{T} centrality estimators, respectively. The kurtosis decreases slightly below $\langle \mathrm{d}N_{\mathrm{ch}}/\mathrm{d}\eta\rangle^{\mathrm{norm}} = 1$ before increasing towards the ultracentral collisions. While the charged-particle multiplicity results show only a modest increase in the ultracentral-collision limit, the E_{T}-based results exhibit a peak around $\langle \mathrm{d}N_{\mathrm{ch}}/\mathrm{d}\eta\rangle^{\mathrm{norm}} \approx 1.1$. The predicted $\kappa_{\langle[p_{\mathrm{T}}]\rangle}^{\mathrm{norm}}$ for both centrality estimators show a dependence on $\langle \mathrm{d}N_{\mathrm{ch}}/\mathrm{d}\eta\rangle^{\mathrm{norm}}$ peaking below $\langle \mathrm{d}N_{\mathrm{ch}}/\mathrm{d}\eta\rangle_{\mathrm{knee}}^{\mathrm{norm}}$, with a shape very different from the relatively flat evolution of the data for the entire $\langle \mathrm{d}N_{\mathrm{ch}}/\mathrm{d}\eta\rangle^{\mathrm{norm}}$.

A key limitation of the model lies in its assumption of a Gaussian distribution of $[p_{\mathrm{T}}]$ at fixed-impact parameter. Since $[p_{\mathrm{T}}]$ is a positive quantity, its distribution is expected to exhibit positive skewness and kurtosis. This inherent property of the $[p_{\mathrm{T}}]$ distribution will contribute to the observed skewness and kurtosis [26].

Figure 8 compares the self-normalized higher-order moments of $[p_{\mathrm{T}}]$ with predictions from the HIJING [42] and Trajectum [55–57] model. Predictions are shown for the N_{ch}- and E_{T}-based centrality estimators at mid-rapidity. Within the independent source picture implemented in the HIJING model, the n^{th}-order cumulant is expected to scale as $\propto 1/N_{\mathrm{ch}}^{(n-1)}$ [62]. However, this approach fails to accurately describe the event-to-event

JHEP11(2025)076

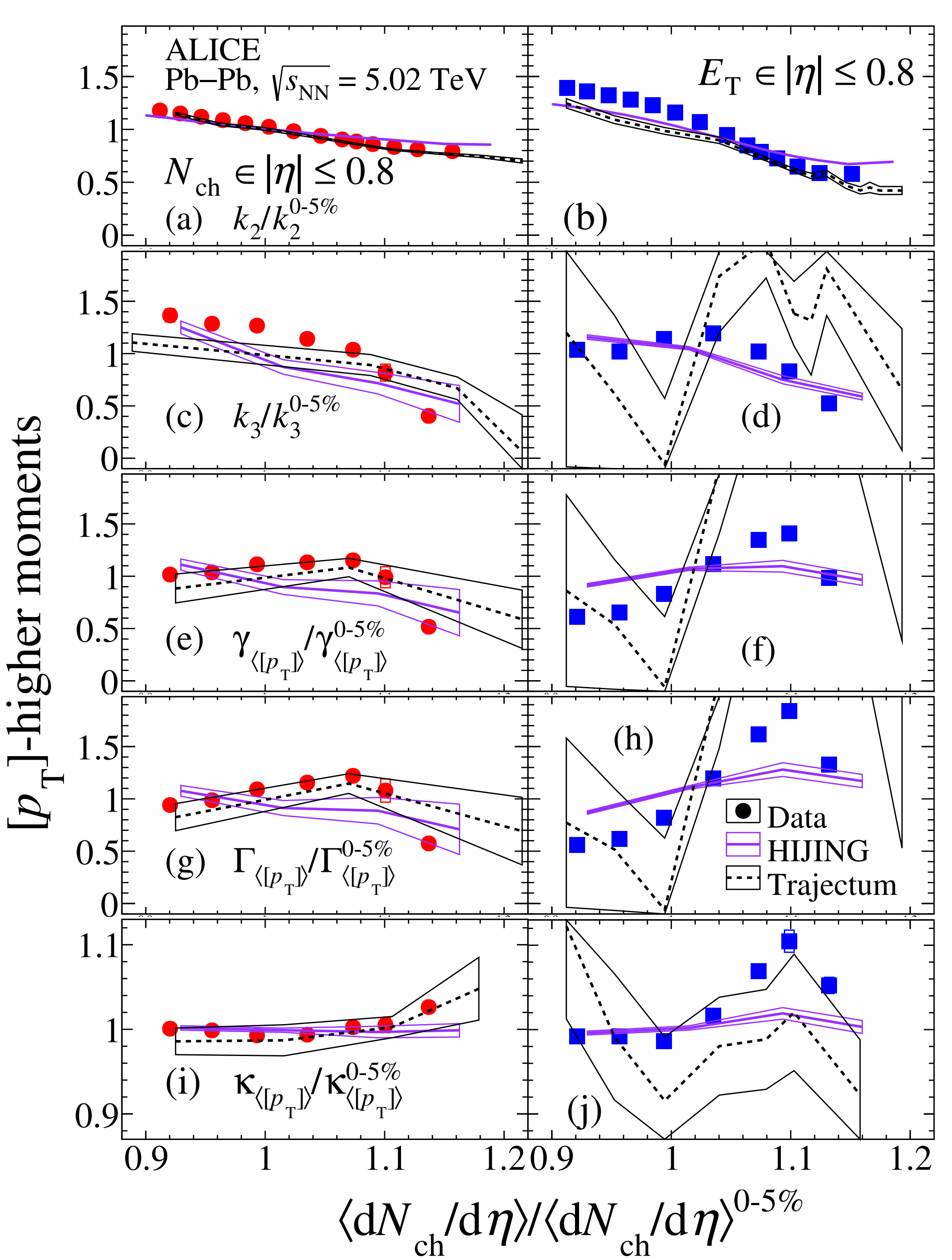

Figure 8. Higher-order moments of $[p_{\rm T}]$ for events selected with the $N_{\rm ch}$ (I) and $E_{\rm T}$ (III) centrality estimators at mid-rapidity in Pb-Pb collisions at $\sqrt{s_{\rm NN}}$ = 5.02 TeV are shown in the left and right columns, respectively. The data are compared with predictions from the HIJING [42] and Trajectum [55–57] models. The width of the bands represents the statistical uncertainty in the HIJING predictions. The bands around the Trajectum predictions represent the sum in quadrature of the statistical and systematic uncertainties, with the latter being the dominant source.

fluctuations of the average transverse momentum observed across the range from peripheral to central collisions [64]. The shape of the predicted $k_2^{\rm norm}$ for both centrality estimators qualitatively agrees with the data. Notably, HIJING predicts a more rapid decrease of $k_2^{\rm norm}$ for $\langle {\rm d}N_{\rm ch}/{\rm d}\eta\rangle^{\rm norm} \gtrsim 1$ with the $E_{\rm T}$-based centrality estimator, similar to what is seen in data. However, the model fails to reproduce the observed bumpy structure in the $k_3^{\rm norm}$, $\gamma_{\langle[p_{\rm T}]\rangle}^{\rm norm}$, and $\Gamma_{\langle[p_{\rm T}]\rangle}^{\rm norm}$ distributions around $\langle {\rm d}N_{\rm ch}/{\rm d}\eta\rangle^{\rm norm} \approx 1.08$. Finally, HIJING agrees with the kurtosis data below $\langle {\rm d}N_{\rm ch}/{\rm d}\eta\rangle^{\rm norm} = 1$ but underestimates the rise in the ultracentral collision regime. The hydrodynamic Trajectum model accurately describes the higher-order $[p_{\rm T}]$ fluctuations for the $N_{\rm ch}$-based centrality estimator and captures the decrease in $k_2^{\rm norm}$, the peaks in $\gamma_{\langle[p_{\rm T}]\rangle}/\gamma_{\langle[p_{\rm T}]\rangle}^{0\text{–}5\%}$ and $\Gamma_{\langle[p_{\rm T}]\rangle}/\Gamma_{\langle[p_{\rm T}]\rangle}^{0\text{–}5\%}$, and the rise in $\kappa_{\langle[p_{\rm T}]\rangle}/\kappa_{\langle[p_{\rm T}]\rangle}^{0\text{–}5\%}$ in ultra-central collisions. The $E_{\rm T}$-based predictions rely on a considerably smaller sample than the $N_{\rm ch}$-based ones. Consequently, the substantial uncertainties in the Trajectum model's predictions for skewness and kurtosis preclude drawing conclusions. Nevertheless, the rapid decrease of $k_2^{\rm norm}$ is well described in the ultracentral-collision limit.

5 Conclusions

This study investigates the dependence of $\langle p_{\rm T}\rangle^{\rm norm}$ on $\langle {\rm d}N_{\rm ch}/{\rm d}\eta\rangle^{\rm norm}$ measured at mid-rapidity in ultracentral Pb-Pb collisions at $\sqrt{s_{\rm NN}} = 5.02$ TeV using different centrality estimators based on $N_{\rm ch}$ and $E_{\rm T}$. Our findings reveal that the $E_{\rm T}$-based centrality estimator leads to a steeper and higher $\langle p_{\rm T}\rangle^{\rm norm}$, potentially influenced by jet-fragmentation biases. Utilizing the $N_{\rm ch}$-based centrality estimator mitigates these biases, and introducing a pseudorapidity gap between the centrality and $\langle p_{\rm T}\rangle^{\rm norm}$ measurement regions further reduces their impact. The extracted $c_{\rm s}^2$ is found to strongly depend on the exploited centrality estimator and ranges between $0.1146 \pm 0.0028\,(\text{stat.}) \pm 0.0065\,(\text{syst.})$ and $0.4374 \pm 0.0006\,(\text{stat.}) \pm 0.0184\,(\text{syst.})$ in natural units. Based on HIJING-model predictions, which show a steady rise of $\langle p_{\rm T}\rangle$ with $\langle N_{\rm ch}\rangle$, the observed increase of $\langle p_{\rm T}\rangle^{\rm norm}$ in the ultracentral-collision limit cannot be solely attributed to fluctuations in the initial state. Consequently, the extracted $c_{\rm s}^2$ may not directly correspond to the speed of sound in the QGP. These measurements confirm a prediction from the Trajectum hydrodynamic model [14], and necessitate a reevaluation of how the speed of sound can be extracted from heavy-ion data.

This study also presents measurements of higher-order moments of $[p_{\rm T}]$ in ultracentral collisions, focusing on comparisons between $N_{\rm ch}$ and $E_{\rm T}$ centrality estimators at mid-rapidity. $k_3^{\rm norm}$, $\gamma_{\langle[p_{\rm T}]\rangle}^{\rm norm}$, and $\Gamma_{\langle[p_{\rm T}]\rangle}^{\rm norm}$ exhibit an increase around $\langle {\rm d}N_{\rm ch}/{\rm d}\eta\rangle^{\rm norm}_{\rm knee}$ followed by a decrease towards the ultracentral-collision limit. These observations deviate from expectations based on independent particle production sources, as implemented in the HIJING model. The two-component model combining Intrinsic and Geometric sources of $[p_{\rm T}]$ fluctuations [26, 27] reproduces most features of the data and suggests that the observed maxima in skewness variables may be attributed to Geometrical fluctuations in the initial state, which vanish in the ultracentral-collision limit.

Acknowledgments

The ALICE collaboration would like to thank all its engineers and technicians for their invaluable contributions to the construction of the experiment and the CERN accelerator teams for the outstanding performance of the LHC complex. The ALICE collaboration gratefully acknowledges the resources and support provided by all Grid centres and the Worldwide LHC Computing Grid (WLCG) collaboration. The ALICE collaboration acknowledges the following funding agencies for their support in building and running the ALICE detector: A.I. Alikhanyan National Science Laboratory (Yerevan Physics Institute) Foundation (ANSL), State Committee of Science and World Federation of Scientists (WFS), Armenia; Austrian Academy of Sciences, Austrian Science Fund (FWF): [M 2467-N36] and Nationalstiftung für Forschung, Technologie und Entwicklung, Austria; Ministry of Communications and High Technologies, National Nuclear Research Center, Azerbaijan; Rede Nacional de Física de Altas Energias (Renafae), Financiadora de Estudos e Projetos (Finep), Fundação de Amparo à Pesquisa do Estado de São Paulo (FAPESP) and The Sao Paulo Research Foundation (FAPESP), Brazil; Bulgarian Ministry of Education and Science, within the National Roadmap for Research Infrastructures 2020–2027 (object CERN), Bulgaria; Ministry of Education of China (MOEC), Ministry of Science & Technology of China (MSTC) and National Natural Science Foundation of China (NSFC), China; Ministry of Science and Education and Croatian Science Foundation, Croatia; Centro de Aplicaciones Tecnológicas y Desarrollo Nuclear (CEADEN), Cubaenergía, Cuba; Ministry of Education, Youth and Sports of the Czech Republic, Czech Republic; The Danish Council for Independent Research | Natural Sciences, the VILLUM FONDEN and Danish National Research Foundation (DNRF), Denmark; Helsinki Institute of Physics (HIP), Finland; Commissariat à l'Energie Atomique (CEA) and Institut National de Physique Nucléaire et de Physique des Particules (IN2P3) and Centre National de la Recherche Scientifique (CNRS), France; Bundesministerium für Bildung und Forschung (BMBF) and GSI Helmholtzzentrum für Schwerionenforschung GmbH, Germany; General Secretariat for Research and Technology, Ministry of Education, Research and Religions, Greece; National Research, Development and Innovation Office, Hungary; Department of Atomic Energy Government of India (DAE), Department of Science and Technology, Government of India (DST), University Grants Commission, Government of India (UGC) and Council of Scientific and Industrial Research (CSIR), India; National Research and Innovation Agency - BRIN, Indonesia; Istituto Nazionale di Fisica Nucleare (INFN), Italy; Japanese Ministry of Education, Culture, Sports, Science and Technology (MEXT) and Japan Society for the Promotion of Science (JSPS) KAKENHI, Japan; Consejo Nacional de Ciencia (CONACYT) y Tecnología, through Fondo de Cooperación Internacional en Ciencia y Tecnología (FONCICYT) and Dirección General de Asuntos del Personal Academico (DGAPA), Mexico; Nederlandse Organisatie voor Wetenschappelijk Onderzoek (NWO), Netherlands; The Research Council of Norway, Norway; Pontificia Universidad Católica del Perú, Peru; Ministry of Science and Higher Education, National Science Centre and WUT ID-UB, Poland; National Research Foundation of Korea (NRF), Republic of Korea; Ministry of Education and Scientific Research, Institute of Atomic Physics, Ministry of Research and Innovation and Institute of Atomic Physics and Universitatea Nationala de Stiinta si Tehnologie Politehnica Bucuresti, Romania; Ministerstvo skolstva, vyskumu, vyvoja a mladeze SR, Slovakia; National Research Foundation of South Africa, South Africa; Swedish Research Council (VR) and Knut & Alice Wallenberg Foundation (KAW), Sweden; European Organization for Nuclear Research, Switzerland; Suranaree University of Technology (SUT), National Science and Technology Development Agency (NSTDA) and National Science, Research and

JHEP11(2025)076

Innovation Fund (NSRF via PMU-B B05F650021), Thailand; Turkish Energy, Nuclear and Mineral Research Agency (TENMAK), Turkey; National Academy of Sciences of Ukraine, Ukraine; Science and Technology Facilities Council (STFC), United Kingdom; National Science Foundation of the United States of America (NSF) and United States Department of Energy, Office of Nuclear Physics (DOE NP), United States of America. In addition, individual groups or members have received support from: Czech Science Foundation (grant no. 23-07499S), Czech Republic; FORTE project, reg. no. CZ.02.01.01/00/22_008/0004632, Czech Republic, co-funded by the European Union, Czech Republic; European Research Council (grant no. 950692), European Union; Deutsche Forschungs Gemeinschaft (DFG, German Research Foundation) "Neutrinos and Dark Matter in Astro- and Particle Physics" (grant no. SFB 1258), Germany; ICSC - National Research Center for High Performance Computing, Big Data and Quantum Computing and FAIR - Future Artificial Intelligence Research, funded by the NextGenerationEU program (Italy).

A $\langle p_{\mathrm{T}}\rangle/\langle p_{\mathrm{T}}\rangle^{0\text{–}5\%}$ as a function of $\langle \mathrm{d}N_{\mathrm{ch}}/\mathrm{d}\eta\rangle/\langle \mathrm{d}N_{\mathrm{ch}}/\mathrm{d}\eta\rangle^{0\text{–}5\%}$ using p_{T} selection

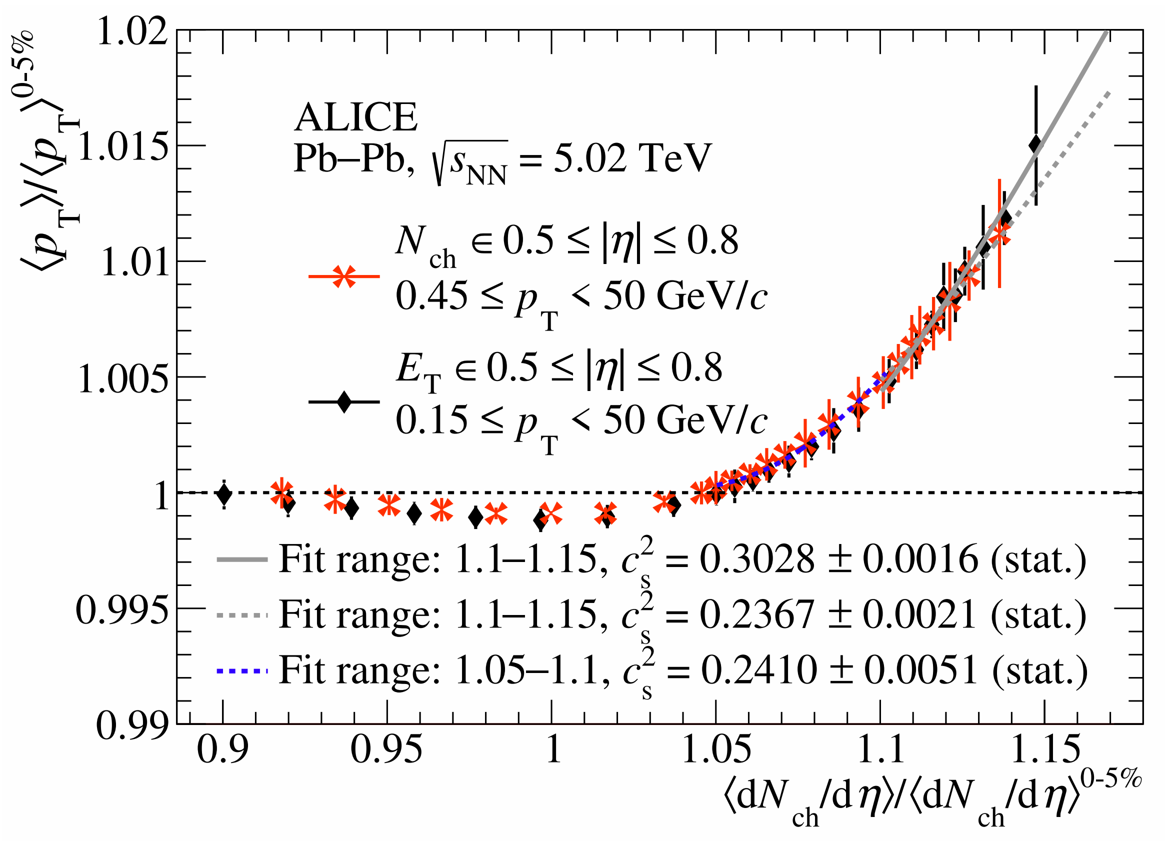

Figure 9. $\langle p_{\mathrm{T}}\rangle^{\mathrm{norm}}$ as a function of $\langle \mathrm{d}N_{\mathrm{ch}}/\mathrm{d}\eta\rangle^{\mathrm{norm}}$. Results are shown for two centrality estimators: one based on transverse energy (black diamonds) and the other based on charged-particle multiplicity (red crosses). For the N_{ch}-based centrality estimator, two values of c_{s}^2 are extracted using non-overlapping fit ranges (dashed-lines). The $\langle p_{\mathrm{T}}\rangle^{\mathrm{norm}}$ versus $\langle \mathrm{d}N_{\mathrm{ch}}/\mathrm{d}\eta\rangle^{\mathrm{norm}}$ correlation for the E_{T}-based centrality estimator corresponds to the centrality definition labeled as IV in table 1.

JHEP11(2025)076

B Higher-order moments of $[p_{\mathrm{T}}]$ moments with the V0M centrality estimator

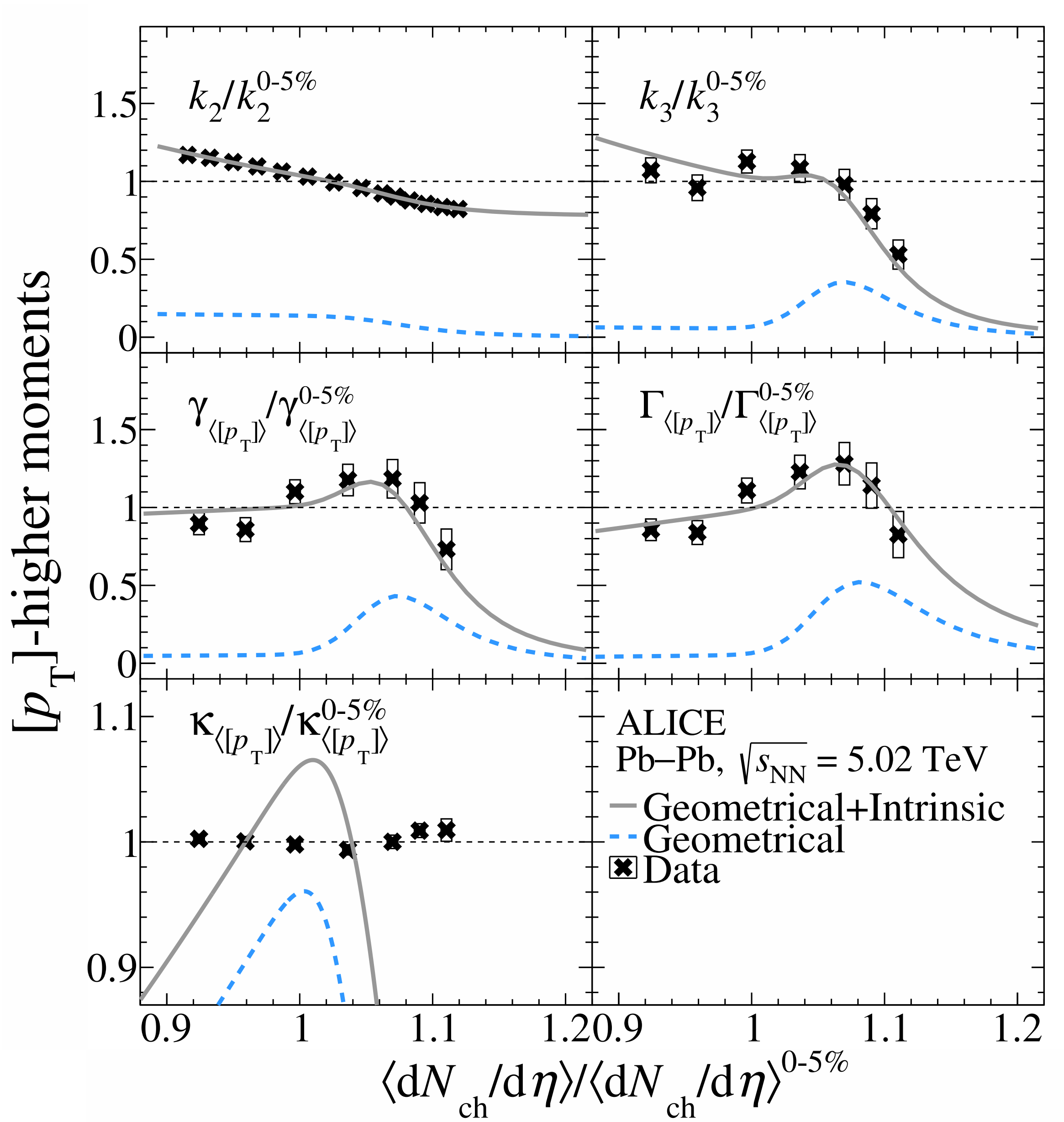

Figure 10. Higher-order moments of $[p_{\mathrm{T}}]$ measured for events selected with the V0 centrality estimator (IX) in Pb-Pb collisions at $\sqrt{s_{\mathrm{NN}}} = 5.02\,\mathrm{TeV}$. The k_2^{norm} distribution is fitted with a two-component model (continuous gray line), where the estimated Geometrical component is also show (dotted-dashed blue line) [27]. The curves for the k_3^{norm}, $\gamma^{\mathrm{norm}}_{\langle[p_{\mathrm{T}}]\rangle}$, $\Gamma^{\mathrm{norm}}_{\langle[p_{\mathrm{T}}]\rangle}$, and $\kappa^{\mathrm{norm}}_{\langle[p_{\mathrm{T}}]\rangle}$ distributions correspond to predictions based on the fit of k_2^{norm} [26].

Data Availability Statement. This article has associated data in a data repository. Available at: https://www.hepdata.net/record/ins2933773.

Code Availability Statement. This article has associated code in a code repository. Available at: https://github.com/alisw/AliRoot and https://github.com/alisw/AliPhysics/.

References

[1] BRAHMS collaboration, *Quark gluon plasma and color glass condensate at RHIC? The Perspective from the BRAHMS experiment*, *Nucl. Phys. A* **757** (2005) 1 [nucl-ex/0410020] [INSPIRE].

[2] PHENIX collaboration, *Formation of dense partonic matter in relativistic nucleus-nucleus collisions at RHIC: Experimental evaluation by the PHENIX collaboration*, *Nucl. Phys. A* **757** (2005) 184 [nucl-ex/0410003] [INSPIRE].

[3] PHOBOS collaboration, *The PHOBOS perspective on discoveries at RHIC*, *Nucl. Phys. A* **757** (2005) 28 [nucl-ex/0410022] [INSPIRE].

[4] STAR collaboration, *Experimental and theoretical challenges in the search for the quark gluon plasma: The STAR Collaboration's critical assessment of the evidence from RHIC collisions*, *Nucl. Phys. A* **757** (2005) 102 [nucl-ex/0501009] [INSPIRE].

[5] ALICE collaboration, *Heavy Ion physics with the ALICE experiment at the CERN LHC*, *Philos. Trans. Roy. Soc. Lond. A* **370** (2012) 917 [arXiv:1109.4291] [INSPIRE].

[6] W. Busza, K. Rajagopal and W. van der Schee, *Heavy Ion Collisions: The Big Picture, and the Big Questions*, *Annu. Rev. Nucl. Part. Sci.* **68** (2018) 339 [arXiv:1802.04801] [INSPIRE].

[7] ALICE collaboration, *The ALICE experiment: a journey through QCD*, *Eur. Phys. J. C* **84** (2024) 813 [arXiv:2211.04384] [INSPIRE].

[8] S. Schlichting and D. Teaney, *The First fm/c of Heavy-Ion Collisions*, *Annu. Rev. Nucl. Part. Sci.* **69** (2019) 447 [arXiv:1908.02113] [INSPIRE].

[9] P. Romatschke and U. Romatschke, *Relativistic Fluid Dynamics In and Out of Equilibrium*, in *Cambridge Monographs on Mathematical Physics*, Cambridge University Press (2019) [arXiv:1712.05815] [DOI:10.1017/9781108651998] [INSPIRE].

[10] J.E. Bernhard, J.S. Moreland and S.A. Bass, *Bayesian estimation of the specific shear and bulk viscosity of quark-gluon plasma*, *Nat. Phys.* **15** (2019) 1113 [INSPIRE].

[11] P. Alba et al., *Effect of the QCD equation of state and strange hadronic resonances on multiparticle correlations in heavy ion collisions*, *Phys. Rev. C* **98** (2018) 034909 [arXiv:1711.05207] [INSPIRE].

[12] A. Mazeliauskas, S. Floerchinger, E. Grossi and D. Teaney, *Fast resonance decays in nuclear collisions*, *Eur. Phys. J. C* **79** (2019) 284 [arXiv:1809.11049] [INSPIRE].

[13] F.G. Gardim, G. Giacalone and J.-Y. Ollitrault, *The mean transverse momentum of ultracentral heavy-ion collisions: A new probe of hydrodynamics*, *Phys. Lett. B* **809** (2020) 135749 [arXiv:1909.11609] [INSPIRE].

[14] G. Nijs and W. van der Schee, *Ultracentral heavy ion collisions, transverse momentum and the equation of state*, Phys. Lett. B **853** (2024) 138636 [arXiv:2312.04623] [INSPIRE].

[15] F.G. Gardim, G. Giacalone, M. Luzum and J.-Y. Ollitrault, *Thermodynamics of hot strong-interaction matter from ultrarelativistic nuclear collisions*, Nat. Phys. **16** (2020) 615 [arXiv:1908.09728] [INSPIRE].

[16] L. Van Hove and S. Pokorski, *High-Energy Hadron-Hadron Collisions and Internal Hadron Structure*, Nucl. Phys. B **86** (1975) 243 [INSPIRE].

[17] HotQCD collaboration, *Equation of state in* $(2+1)$*-flavor QCD*, Phys. Rev. D **90** (2014) 094503 [arXiv:1407.6387] [INSPIRE].

[18] P. Braun-Munzinger, V. Koch, T. Schäfer and J. Stachel, *Properties of hot and dense matter from relativistic heavy ion collisions*, Phys. Rep. **621** (2016) 76 [arXiv:1510.00442] [INSPIRE].

[19] J.-Y. Ollitrault, *Relativistic hydrodynamics for heavy-ion collisions*, Eur. J. Phys. **29** (2008) 275 [arXiv:0708.2433] [INSPIRE].

[20] L. Van Hove, *Multiplicity Dependence of* p_t *Spectrum as a Possible Signal for a Phase Transition in Hadronic Collisions*, Phys. Lett. B **118** (1982) 138 [INSPIRE].

[21] CMS collaboration, *Extracting the speed of sound in quark-gluon plasma with ultrarelativistic lead-lead collisions at the LHC*, Rept. Prog. Phys. **87** (2024) 077801 [arXiv:2401.06896] [INSPIRE].

[22] ATLAS collaboration, *Disentangling Sources of Momentum Fluctuations in Xe+Xe and Pb+Pb Collisions with the ATLAS Detector*, Phys. Rev. Lett. **133** (2024) 252301 [arXiv:2407.06413] [INSPIRE].

[23] P. Bozek and W. Broniowski, *Transverse-momentum fluctuations in relativistic heavy-ion collisions from event-by-event viscous hydrodynamics*, Phys. Rev. C **85** (2012) 044910 [arXiv:1203.1810] [INSPIRE].

[24] P. Bożek and W. Broniowski, *Transverse momentum fluctuations in ultrarelativistic Pb + Pb and p + Pb collisions with "wounded" quarks*, Phys. Rev. C **96** (2017) 014904 [arXiv:1701.09105] [INSPIRE].

[25] ALICE collaboration, *Transverse momentum spectra and nuclear modification factors of charged particles in pp, p-Pb and Pb-Pb collisions at the LHC*, JHEP **11** (2018) 013 [arXiv:1802.09145] [INSPIRE].

[26] R. Samanta, J.P. Picchetti, M. Luzum and J.-Y. Ollitrault, *Non-Gaussian transverse momentum fluctuations from impact parameter fluctuations*, Phys. Rev. C **108** (2023) 024908 [arXiv:2306.09294] [INSPIRE].

[27] R. Samanta et al., *Thermalization at the femtoscale seen in high-energy Pb+Pb collisions*, Phys. Rev. C **109** (2024) L051902 [arXiv:2303.15323] [INSPIRE].

[28] W. Broniowski, M. Chojnacki and L. Obara, *Size fluctuations of the initial source and the event-by-event transverse momentum fluctuations in relativistic heavy-ion collisions*, Phys. Rev. C **80** (2009) 051902 [arXiv:0907.3216] [INSPIRE].

[29] ALICE collaboration, *Skewness and kurtosis of mean transverse momentum fluctuations at the LHC energies*, Phys. Lett. B **850** (2024) 138541 [arXiv:2308.16217] [INSPIRE].

[30] F.G. Gardim, A.V. Giannini and J.-Y. Ollitrault, *Accessing the speed of sound in relativistic ultracentral nucleus-nucleus collisions using the mean transverse momentum*, Phys. Lett. B **856** (2024) 138937 [arXiv:2403.06052] [INSPIRE].

[31] ALICE collaboration, *The ALICE experiment at the CERN LHC*, 2008 *JINST* **3** S08002 [INSPIRE].

[32] ALICE collaboration, *Performance of the ALICE Experiment at the CERN LHC*, *Int. J. Mod. Phys. A* **29** (2014) 1430044 [arXiv:1402.4476] [INSPIRE].

[33] ALICE collaboration, *Performance of the ALICE VZERO system*, 2013 *JINST* **8** P10016 [arXiv:1306.3130] [INSPIRE].

[34] ALICE collaboration, *Alignment of the ALICE Inner Tracking System with cosmic-ray tracks*, 2010 *JINST* **5** P03003 [arXiv:1001.0502] [INSPIRE].

[35] J. Alme et al., *The ALICE TPC, a large 3-dimensional tracking device with fast readout for ultra-high multiplicity events*, *Nucl. Instrum. Meth. A* **622** (2010) 316 [arXiv:1001.1950] [INSPIRE].

[36] R. Arnaldi et al., *The Zero degree calorimeters for the ALICE experiment*, *Nucl. Instrum. Meth. A* **581** (2007) 397 [*Erratum ibid.* **604** (2009) 765] [INSPIRE].

[37] R. Arnaldi et al., *Physics performance of the ALICE zero degree calorimeter*, *Nucl. Phys. B Proc. Suppl.* **197** (2009) 206 [INSPIRE].

[38] ALICE collaboration, *Centrality determination of Pb-Pb collisions at* $\sqrt{s_{\rm NN}} = 2.76$ *TeV with ALICE*, *Phys. Rev. C* **88** (2013) 044909 [arXiv:1301.4361] [INSPIRE].

[39] ALICE collaboration, *The ALICE definition of primary particles*, ALICE-PUBLIC-2017-005 (2017).

[40] ALICE collaboration, *Proton emission in ultraperipheral Pb-Pb collisions at* $\sqrt{s_{\rm NN}} = 5.02$ *TeV*, *Phys. Rev. C* **111** (2025) 054906 [arXiv:2411.07058] [INSPIRE].

[41] ALICE collaboration, *Centrality Dependence of the Charged-Particle Multiplicity Density at Midrapidity in Pb-Pb Collisions at* $\sqrt{s_{\rm NN}} = 5.02$ *TeV*, *Phys. Rev. Lett.* **116** (2016) 222302 [arXiv:1512.06104] [INSPIRE].

[42] X.-N. Wang and M. Gyulassy, *HIJING: A Monte Carlo model for multiple jet production in pp, pA and AA collisions*, *Phys. Rev. D* **44** (1991) 3501 [INSPIRE].

[43] R. Brun et al., *GEANT 3: user's guide Geant 3.10, Geant 3.11*, rev. version, CERN-DD-EE-84-01, CERN, Geneva (1987).

[44] ALICE collaboration, *Production of charged pions, kaons, and (anti-)protons in Pb-Pb and inelastic pp collisions at* $\sqrt{s_{\rm NN}} = 5.02$ *TeV*, *Phys. Rev. C* **101** (2020) 044907 [arXiv:1910.07678] [INSPIRE].

[45] ALICE collaboration, *Multiplicity dependence of* π*, K, and p production in pp collisions at* $\sqrt{s} = 13$ *TeV*, *Eur. Phys. J. C* **80** (2020) 693 [arXiv:2003.02394] [INSPIRE].

[46] E. Schnedermann, J. Sollfrank and U.W. Heinz, *Thermal phenomenology of hadrons from* 200 *A/GeV S+S collisions*, *Phys. Rev. C* **48** (1993) 2462 [nucl-th/9307020] [INSPIRE].

[47] E.G.D. Nielsen, F.K. Rømer, K. Gulbrandsen and Y. Zhou, *Generic multi-particle transverse momentum correlations as a new tool for studying nuclear structure at the energy frontier*, *Eur. Phys. J. A* **60** (2024) 38 [arXiv:2312.00492] [INSPIRE].

[48] ALICE collaboration, *Systematic study of flow vector fluctuations in* $\sqrt{s_{\rm NN}} = 5.02$ *TeV Pb-Pb collisions*, *Phys. Rev. C* **109** (2024) 065202 [arXiv:2403.15213] [INSPIRE].

[49] B. Efron, *Bootstrap Methods: Another Look at the Jackknife*, *Ann. Statist.* **7** (1979) 1 [INSPIRE].

[50] R. Barlow, *Systematic errors: Facts and fictions*, in the proceedings of the *Conference on Advanced Statistical Techniques in Particle Physics*, Durham, U.K., 18–22 March 2002, pp. 134–144 [hep-ex/0207026] [INSPIRE].

[51] G. Wilk and Z. Wlodarczyk, *On the interpretation of nonextensive parameter q in Tsallis statistics and Levy distributions*, Phys. Rev. Lett. **84** (2000) 2770 [hep-ph/9908459] [INSPIRE].

[52] R. Hagedorn, *Multiplicities, p_T Distributions and the Expected Hadron $\to$ Quark-Gluon Phase Transition*, Riv. Nuovo Cim. **6N10** (1983) 1 [INSPIRE].

[53] ALICE collaboration, *Centrality dependence of the nuclear modification factor of charged pions, kaons, and protons in Pb-Pb collisions at $\sqrt{s_{\rm NN}} = 2.76$ TeV*, Phys. Rev. C **93** (2016) 034913 [arXiv:1506.07287] [INSPIRE].

[54] S.J. Das, G. Giacalone, P.-A. Monard and J.-Y. Ollitrault, *Relating centrality to impact parameter in nucleus-nucleus collisions*, Phys. Rev. C **97** (2018) 014905 [arXiv:1708.00081] [INSPIRE].

[55] G. Nijs and W. van der Schee, *A generalized hydrodynamizing initial stage for Heavy Ion Collisions*, arXiv:2304.06191 [INSPIRE].

[56] G. Nijs, W. van der Schee, U. Gürsoy and R. Snellings, *Bayesian analysis of heavy ion collisions with the heavy ion computational framework Trajectum*, Phys. Rev. C **103** (2021) 054909 [arXiv:2010.15134] [INSPIRE].

[57] G. Nijs and W. van der Schee, *Predictions and postdictions for relativistic lead and oxygen collisions with the computational simulation code Trajectum*, Phys. Rev. C **106** (2022) 044903 [arXiv:2110.13153] [INSPIRE].

[58] J.S. Moreland, J.E. Bernhard and S.A. Bass, *Alternative ansatz to wounded nucleon and binary collision scaling in high-energy nuclear collisions*, Phys. Rev. C **92** (2015) 011901 [arXiv:1412.4708] [INSPIRE].

[59] SMASH collaboration, *Particle production and equilibrium properties within a new hadron transport approach for heavy-ion collisions*, Phys. Rev. C **94** (2016) 054905 [arXiv:1606.06642] [INSPIRE].

[60] S. Chatterjee and P. Bozek, *Pseudorapidity profile of transverse momentum fluctuations in heavy ion collisions*, Phys. Rev. C **96** (2017) 014906 [arXiv:1704.02777] [INSPIRE].

[61] G. Giacalone, F.G. Gardim, J. Noronha-Hostler and J.-Y. Ollitrault, *Skewness of mean transverse momentum fluctuations in heavy-ion collisions*, Phys. Rev. C **103** (2021) 024910 [arXiv:2004.09799] [INSPIRE].

[62] S. Bhatta, C. Zhang and J. Jia, *Higher-order transverse momentum fluctuations in heavy-ion collisions*, Phys. Rev. C **105** (2022) 024904 [arXiv:2112.03397] [INSPIRE].

[63] ALICE collaboration, *Transverse momentum spectra and nuclear modification factors of charged particles in Xe-Xe collisions at $\sqrt{s_{\rm NN}} = 5.44$ TeV*, Phys. Lett. B **788** (2019) 166 [arXiv:1805.04399] [INSPIRE].

[64] ALICE collaboration, *Event-by-event mean p_T fluctuations in pp and Pb-Pb collisions at the LHC*, Eur. Phys. J. C **74** (2014) 3077 [arXiv:1407.5530] [INSPIRE].

[65] ALICE collaboration, *Study of $\langle p_T \rangle$ and its higher moments, and extraction of the speed of sound in Pb-Pb collisions with ALICE*, https://www.hepdata.net/record/ins2933773.

[66] https://github.com/alisw/AliRoot.

[67] https://github.com/alisw/AliPhysics/.

The ALICE collaboration

I.J. Abualrob[113], S. Acharya[50], G. Aglieri Rinella[32], L. Aglietta[24], M. Agnello[29], N. Agrawal[25], Z. Ahammed[132], S. Ahmad[15], I. Ahuja[36], Z. Akbar[80], A. Akindinov[138], V. Akishina[38], M. Al-Turany[95], D. Aleksandrov[138], B. Alessandro[56], H.M. Alfanda[6], R. Alfaro Molina[67], B. Ali[15], A. Alici[25], A. Alkin[102], J. Alme[20], G. Alocco[24], T. Alt[64], A.R. Altamura[50], I. Altsybeev[93], C. Andrei[45], N. Andreou[112], A. Andronic[123], E. Andronov[138], V. Anguelov[92], F. Antinori[54], P. Antonioli[51], N. Apadula[72], H. Appelshäuser[64], C. Arata[71], S. Arcelli[25], R. Arnaldi[56], J.G.M.C.A. Arneiro[108], I.C. Arsene[19], M. Arslandok[135], A. Augustinus[32], R. Averbeck[95], D. Averyanov[138], M.D. Azmi[15], H. Baba[121], A.R.J. Babu[134], A. Badalà[53], J. Bae[102], Y. Bae[102], Y.W. Baek[40], X. Bai[117], R. Bailhache[64], Y. Bailung[48], R. Bala[89], A. Baldisseri[127], B. Balis[2], S. Bangalia[115], Z. Banoo[89], V. Barbasova[36], F. Barile[31], L. Barioglio[56], M. Barlou[24,76], B. Barman[41], G.G. Barnaföldi[46], L.S. Barnby[112], E. Barreau[101], V. Barret[124], L. Barreto[108], K. Barth[32], E. Bartsch[64], N. Bastid[124], S. Basu[I,73], G. Batigne[101], D. Battistini[93], B. Batyunya[139], D. Bauri[47], J.L. Bazo Alba[99], I.G. Bearden[81], P. Becht[95], D. Behera[48], I. Belikov[126], V.D. Bella[126], F. Bellini[25], R. Bellwied[113], S. Belokurova[138], L.G.E. Beltran[107], Y.A.V. Beltran[44], G. Bencedi[46], A. Bensaoula[113], S. Beole[24], Y. Berdnikov[138], A. Berdnikova[92], L. Bergmann[92], L. Bernardinis[23], L. Betev[32], P.P. Bhaduri[132], T. Bhalla[88], A. Bhasin[89], B. Bhattacharjee[41], S. Bhattarai[115], L. Bianchi[24], J. Bielčík[34], J. Bielčíková[84], A. Bilandzic[93], A. Binoy[115], G. Biro[46], S. Biswas[4], D. Blau[138], M.B. Blidaru[95], N. Bluhme[38], C. Blume[64], F. Bock[85], T. Bodova[20], J. Bok[16], L. Boldizsár[46], M. Bombara[36], P.M. Bond[32], G. Bonomi[131,55], H. Borel[127], A. Borissov[138], A.G. Borquez Carcamo[92], E. Botta[24], Y.E.M. Bouziani[64], D.C. Brandibur[63], L. Bratrud[64], P. Braun-Munzinger[95], M. Bregant[108], M. Broz[34], G.E. Bruno[94,31], V.D. Buchakchiev[35], M.D. Buckland[83], D. Budnikov[138], H. Buesching[64], S. Bufalino[29], P. Buhler[100], N. Burmasov[139], Z. Buthelezi[68,120], A. Bylinkin[20], C. Carr[98], J.C. Cabanillas Noris[107], M.F.T. Cabrera[113], H. Caines[135], A. Caliva[28], E. Calvo Villar[99], J.M.M. Camacho[107], P. Camerini[23], M.T. Camerlingo[50], F.D.M. Canedo[108], S. Cannito[23], S.L. Cantway[135], M. Carabas[111], F. Carnesecchi[32], L.A.D. Carvalho[108], J. Castillo Castellanos[127], M. Castoldi[32], F. Catalano[32], S. Cattaruzzi[23], R. Cerri[24], I. Chakaberia[72], P. Chakraborty[133], J.W.O. Chan[113], S. Chandra[132], S. Chapeland[32], M. Chartier[116], S. Chattopadhay[132], M. Chen[39], T. Cheng[6], C. Cheshkov[125], D. Chiappara[27], V. Chibante Barroso[32], D.D. Chinellato[100], F. Chinu[24], E.S. Chizzali[II,93], J. Cho[58], S. Cho[58], P. Chochula[32], Z.A. Chochulska[133], D. Choudhury[41], P. Christakoglou[82], C.H. Christensen[81], P. Christiansen[73], T. Chujo[122], M. Ciacco[29], C. Cicalo[52], G. Cimador[24], F. Cindolo[51], M.R. Ciupek[95], G. Clai[III,51], F. Colamaria[50], J.S. Colburn[98], D. Colella[31], A. Colelli[31], M. Colocci[25], M. Concas[32], G. Conesa Balbastre[71], Z. Conesa del Valle[128], G. Contin[23], J.G. Contreras[34], M.L. Coquet[101], P. Cortese[130,56], M.R. Cosentino[110], F. Costa[32], S. Costanza[21], P. Crochet[124], M.M. Czarnynoga[133], A. Dainese[54], G. Dange[38], M.C. Danisch[92], A. Danu[63], P. Das[32], S. Das[4], A.R. Dash[123], S. Dash[47], A. De Caro[28], G. de Cataldo[50], J. de Cuveland[38], A. De Falco[22], D. De Gruttola[28], N. De Marco[56], C. De Martin[23], S. De Pasquale[28],

JHEP11(2025)076

R. Deb[131], R. Del Grande[93], L. Dello Stritto[32], G.G.A. de Souza[IV,108], P. Dhankher[18], D. Di Bari[31], M. Di Costanzo[29], A. Di Mauro[32], B. Di Ruzza[129], B. Diab[32], Y. Ding[6], J. Ditzel[64], R. Divià[32], Ø. Djuvsland[20], U. Dmitrieva[138], A. Dobrin[63], B. Dönigus[64], L. Döpper[42], J.M. Dubinski[133], A. Dubla[95], P. Dupieux[124], N. Dzalaiova[13], T.M. Eder[123], R.J. Ehlers[72], F. Eisenhut[64], R. Ejima[90], D. Elia[50], B. Erazmus[101], F. Ercolessi[25], B. Espagnon[128], G. Eulisse[32], D. Evans[98], S. Evdokimov[138], L. Fabbietti[93], M. Faggin[32], J. Faivre[71], F. Fan[6], W. Fan[72], T. Fang[6], A. Fantoni[49], M. Fasel[85], G. Feofilov[138], A. Fernández Téllez[44], L. Ferrandi[108], M.B. Ferrer[32], A. Ferrero[127], C. Ferrero[V,56], A. Ferretti[24], V.J.G. Feuillard[92], D. Finogeev[138], F.M. Fionda[52], A.N. Flores[106], S. Foertsch[68], I. Fokin[92], S. Fokin[138], U. Follo[V,56], R. Forynski[112], E. Fragiacomo[57], E. Frajna[46], H. Fribert[93], U. Fuchs[32], N. Funicello[28], C. Furget[71], A. Furs[138], T. Fusayasu[96], J.J. Gaardhøje[81], M. Gagliardi[24], A.M. Gago[99], T. Gahlaut[47], C.D. Galvan[107], S. Gami[78], D.R. Gangadharan[113], P. Ganoti[76], C. Garabatos[95], J.M. Garcia[44], T. García Chávez[44], E. Garcia-Solis[9], S. Garetti[128], C. Gargiulo[32], P. Gasik[95], H.M. Gaur[38], A. Gautam[115], M.B. Gay Ducati[66], M. Germain[101], R.A. Gernhaeuser[93], C. Ghosh[132], M. Giacalone[51], G. Gioachin[29], S.K. Giri[132], P. Giubellino[95,56], P. Giubilato[27], P. Glässel[92], E. Glimos[119], V. Gonzalez[134], P. Gordeev[138], M. Gorgon[2], K. Goswami[48], S. Gotovac[33], V. Grabski[67], L.K. Graczykowski[133], E. Grecka[84], A. Grelli[59], C. Grigoras[32], V. Grigoriev[138], S. Grigoryan[139,1], O.S. Groettvik[32], F. Grosa[32], J.F. Grosse-Oetringhaus[32], R. Grosso[95], D. Grund[34], N.A. Grunwald[92], R. Guernane[71], M. Guilbaud[101], K. Gulbrandsen[81], J.K. Gumprecht[100], T. Gündem[64], T. Gunji[121], J. Guo[10], W. Guo[6], A. Gupta[89], R. Gupta[89], R. Gupta[48], K. Gwizdziel[133], L. Gyulai[46], C. Hadjidakis[128], F.U. Haider[89], S. Haidlova[34], M. Haldar[4], H. Hamagaki[74], Y. Han[137], B.G. Hanley[134], R. Hannigan[106], J. Hansen[73], J.W. Harris[135], A. Harton[9], M.V. Hartung[64], H. Hassan[114], D. Hatzifotiadou[51], P. Hauer[42], L.B. Havener[135], E. Hellbär[32], H. Helstrup[37], M. Hemmer[64], T. Herman[34], S.G. Hernandez[113], G. Herrera Corral[8], K.F. Hetland[37], B. Heybeck[64], H. Hillemanns[32], B. Hippolyte[126], I.P.M. Hobus[82], F.W. Hoffmann[70], B. Hofman[59], M. Horst[93], A. Horzyk[2], Y. Hou[95,6], P. Hristov[32], P. Huhn[64], L.M. Huhta[114], T.J. Humanic[86], V. Humlova[34], A. Hutson[113], D. Hutter[38], M.C. Hwang[18], R. Ilkaev[138], M. Inaba[122], M. Ippolitov[138], A. Isakov[82], T. Isidori[115], M.S. Islam[47], S. Iurchenko[138], M. Ivanov[13], M. Ivanov[95], V. Ivanov[138], K.E. Iversen[73], J.G.Kim[137], M. Jablonski[2], B. Jacak[18,72], N. Jacazio[25], P.M. Jacobs[72], S. Jadlovska[104], J. Jadlovsky[104], S. Jaelani[80], C. Jahnke[109], M.J. Jakubowska[133], M.A. Janik[133], S. Ji[16], S. Jia[81], T. Jiang[10], A.A.P. Jimenez[65], S. Jin[10], F. Jonas[72], D.M. Jones[116], J.M. Jowett [32,95], J. Jung[64], M. Jung[64], A. Junique[32], A. Jusko[98], J. Kaewjai[103], P. Kalinak[60], A. Kalweit[32], A. Karasu Uysal[136], N. Karatzenis[98], O. Karavichev[138], T. Karavicheva[138], E. Karpechev[138], M.J. Karwowska[133], U. Kebschull[70], M. Keil[32], B. Ketzer[42], J. Keul[64], S.S. Khade[48], A.M. Khan[117], A. Khanzadeev[138], Y. Kharlov[138], A. Khatun[115], A. Khuntia[51], Z. Khuranova[64], B. Kileng[37], B. Kim[102], C. Kim[16], D.J. Kim[114], D. Kim[102], E.J. Kim[69], G. Kim[58], H. Kim[58], J. Kim[137], J. Kim[58], J. Kim[32], M. Kim[18], S. Kim[17], T. Kim[137], K. Kimura[90], S. Kirsch[64], I. Kisel[38], S. Kiselev[138], A. Kisiel[133], J.L. Klay[5], J. Klein[32], S. Klein[72], C. Klein-Bösing[123],

M. Kleiner[64], A. Kluge[32], C. Kobdaj[103], R. Kohara[121], T. Kollegger[95], A. Kondratyev[139], N. Kondratyeva[138], J. Konig[64], P.J. Konopka[32], G. Kornakov[133], M. Korwieser[93], S.D. Koryciak[2], C. Koster[82], A. Kotliarov[84], N. Kovacic[87], V. Kovalenko[138], M. Kowalski[105], V. Kozhuharov[35], G. Kozlov[38], I. Králik[60], A. Kravčáková[36], L. Krcal[32], M. Krivda[98,60], F. Krizek[84], K. Krizkova Gajdosova[34], C. Krug[66], D.M. Krupova[34], E. Kryshen[138], V. Kučera[58], C. Kuhn[126], T. Kumaoka[122], D. Kumar[132], L. Kumar[88], N. Kumar[88], S. Kumar[50], S. Kundu[32], M. Kuo[122], P. Kurashvili[77], A.B. Kurepin[138], S. Kurita[90], A. Kuryakin[138], S. Kushpil[84], V. Kuskov[138], M. Kutyla[133], A. Kuznetsov[139], M.J. Kweon[58], Y. Kwon[137], S.L. La Pointe[38], P. La Rocca[26], A. Lakrathok[103], M. Lamanna[32], S. Lambert[101], A.R. Landou[71], R. Langoy[118], P. Larionov[32], E. Laudi[32], L. Lautner[93], R.A.N. Laveaga[107], R. Lavicka[100], R. Lea[131,55], H. Lee[102], I. Legrand[45], G. Legras[123], A.M. Lejeune[34], T.M. Lelek[2], R.C. Lemmon[I,83], I. León Monzón[107], M.M. Lesch[93], P. Lévai[46], M. Li[6], P. Li[10], X. Li[10], B.E. Liang-Gilman[18], J. Lien[118], R. Lietava[98], I. Likmeta[113], B. Lim[56], H. Lim[16], S.H. Lim[16], S. Lin[10], V. Lindenstruth[38], C. Lippmann[95], D. Liskova[104], D.H. Liu[6], J. Liu[116], G.S.S. Liveraro[109], I.M. Lofnes[20], C. Loizides[85], S. Lokos[105], J. Lömker[59], X. Lopez[124], E. López Torres[7], C. Lotteau[125], P. Lu[95,117], W. Lu[6], Z. Lu[10], F.V. Lugo[67], J. Luo[39], G. Luparello[57], M.A.T. Johnson[44], Y.G. Ma[39], M. Mager[32], A. Maire[126], E.M. Majerz[2], M.V. Makariev[35], M. Malaev[138], G. Malfattore[51], N.M. Malik[89], N. Malik[15], S.K. Malik[89], D. Mallick[128], N. Mallick[114], G. Mandaglio[30,53], S.K. Mandal[77], A. Manea[63], V. Manko[138], A.K. Manna[48], F. Manso[124], G. Mantzaridis[93], V. Manzari[50], Y. Mao[6], R.W. Marcjan[2], G.V. Margagliotti[23], A. Margotti[51], A. Marín[95], C. Markert[106], P. Martinengo[32], M.I. Martínez[44], G. Martínez García[101], M.P.P. Martins[32,108], S. Masciocchi[95], M. Masera[24], A. Masoni[52], L. Massacrier[128], O. Massen[59], A. Mastroserio[129,50], L. Mattei[24,124], S. Mattiazzo[27], A. Matyja[105], F. Mazzaschi[32], M. Mazzilli[31,113], Y. Melikyan[43], M. Melo[108], A. Menchaca-Rocha[67], J.E.M. Mendez[65], E. Meninno[100], A.S. Menon[113], M.W. Menzel[32,92], M. Meres[13], L. Micheletti[56], D. Mihai[111], D.L. Mihaylov[93], A.U. Mikalsen[20], K. Mikhaylov[139,138], L. Millot[71], N. Minafra[115], D. Miśkowiec[95], A. Modak[57,131], B. Mohanty[78], M. Mohisin Khan[VI,15], M.A. Molander[43], M.M. Mondal[78], S. Monira[133], D.A. Moreira De Godoy[123], I. Morozov[138], A. Morsch[32], T. Mrnjavac[32], S. Mrozinski[64], V. Muccifora[49], S. Muhuri[132], A. Mulliri[22], M.G. Munhoz[108], R.H. Munzer[64], H. Murakami[121], L. Musa[32], J. Musinsky[60], J.W. Myrcha[133], B. Naik[120], A.I. Nambrath[18], B.K. Nandi[47], R. Nania[51], E. Nappi[50], A.F. Nassirpour[17], V. Nastase[111], A. Nath[92], N.F. Nathanson[81], C. Nattrass[119], K. Naumov[18], A. Neagu[19], L. Nellen[65], R. Nepeivoda[73], S. Nese[19], N. Nicassio[31], B.S. Nielsen[81], E.G. Nielsen[81], S. Nikolaev[138], V. Nikulin[138], F. Noferini[51], S. Noh[12], P. Nomokonov[139], J. Norman[116], N. Novitzky[85], J. Nystrand[20], M.R. Ockleton[116], M. Ogino[74], S. Oh[17], A. Ohlson[73], M. Oida[90], V.A. Okorokov[138], J. Oleniacz[133], C. Oppedisano[56], A. Ortiz Velasquez[65], H. Osanai[74], J. Otwinowski[105], M. Oya[90], K. Oyama[74], S. Padhan[47], D. Pagano[131,55], G. Paić[65], S. Paisano-Guzmán[44], A. Palasciano[50], I. Panasenko[73], S. Panebianco[127], P. Panigrahi[47], C. Pantouvakis[27], H. Park[122], J. Park[122], S. Park[102], T.Y. Park[137], J.E. Parkkila[133], P.B. Pati[81], Y. Patley[47], R.N. Patra[50], P. Paudel[115], B. Paul[132], H. Pei[6],

T. Peitzmann[59], X. Peng[11], M. Pennisi[24], S. Perciballi[24], D. Peresunko[138], G.M. Perez[7], Y. Pestov[138], V. Petrov[138], M. Petrovici[45], S. Piano[57], M. Pikna[13], P. Pillot[101], O. Pinazza[51,32], L. Pinsky[113], C. Pinto[32], S. Pisano[49], M. Płoskoń[72], M. Planinic[87], D.K. Plociennik[2], M.G. Poghosyan[85], B. Polichtchouk[138], S. Politano[32,24], N. Poljak[87], A. Pop[45], S. Porteboeuf-Houssais[124], I.Y. Pozos[44], K.K. Pradhan[48], S.K. Prasad[4], S. Prasad[48], R. Preghenella[51], F. Prino[56], C.A. Pruneau[134], I. Pshenichnov[138], M. Puccio[32], S. Pucillo[28,24], L. Quaglia[24], A.M.K. Radhakrishnan[48], S. Ragoni[14], A. Rai[135], A. Rakotozafindrabe[127], N. Ramasubramanian[125], L. Ramello[130,56], C.O. Ramírez-Álvarez[44], M. Rasa[26], S.S. Räsänen[43], M.P. Rauch[20], I. Ravasenga[32], K.F. Read[85,119], C. Reckziegel[110], A.R. Redelbach[38], K. Redlich[VII,77], C.A. Reetz[95], H.D. Regules-Medel[44], A. Rehman[20], F. Reidt[32], H.A. Reme-Ness[37], K. Reygers[92], V. Riabov[138], R. Ricci[28], M. Richter[20], A.A. Riedel[93], W. Riegler[32], A.G. Riffero[24], M. Rignanese[27], C. Ripoli[28], C. Ristea[63], M.V. Rodriguez[32], M. Rodríguez Cahuantzi[44], K. Røed[19], R. Rogalev[138], E. Rogochaya[139], D. Rohr[32], D. Röhrich[20], S. Rojas Torres[34], P.S. Rokita[133], G. Romanenko[25], F. Ronchetti[32], D. Rosales Herrera[44], E.D. Rosas[65], K. Roslon[133], A. Rossi[54], A. Roy[48], S. Roy[47], N. Rubini[51], J.A. Rudolph[82], D. Ruggiano[133], R. Rui[23], P.G. Russek[2], R. Russo[82], A. Rustamov[79], E. Ryabinkin[138], Y. Ryabov[138], A. Rybicki[105], L.C.V. Ryder[115], J. Ryu[16], W. Rzesa[133], B. Sabiu[51], S. Sadhu[42], S. Sadovsky[138], J. Saetre[20], S. Saha[78], B. Sahoo[48], R. Sahoo[48], D. Sahu[48], P.K. Sahu[61], J. Saini[132], K. Sajdakova[36], S. Sakai[122], S. Sambyal[89], D. Samitz[100], I. Sanna[32,93], T.B. Saramela[108], D. Sarkar[81], P. Sarma[41], V. Sarritzu[22], V.M. Sarti[93], M.H.P. Sas[32], S. Sawan[78], E. Scapparone[51], J. Schambach[85], H.S. Scheid[32], C. Schiaua[45], R. Schicker[92], F. Schlepper[32,92], A. Schmah[95], C. Schmidt[95], M.O. Schmidt[32], M. Schmidt[91], N.V. Schmidt[85], A.R. Schmier[119], J. Schoengarth[64], R. Schotter[100], A. Schröter[38], J. Schukraft[32], K. Schweda[95], G. Scioli[25], E. Scomparin[56], J.E. Seger[14], Y. Sekiguchi[121], D. Sekihata[121], M. Selina[82], I. Selyuzhenkov[95], S. Senyukov[126], J.J. Seo[92], D. Serebryakov[138], L. Serkin[VIII,65], L. Šerkšnytė[93], A. Sevcenco[63], T.J. Shaba[68], A. Shabetai[101], R. Shahoyan[32], A. Shangaraev[138], B. Sharma[89], D. Sharma[47], H. Sharma[54], M. Sharma[89], S. Sharma[89], T. Sharma[41], U. Sharma[89], A. Shatat[128], O. Sheibani[134], K. Shigaki[90], M. Shimomura[75], S. Shirinkin[138], Q. Shou[39], Y. Sibiriak[138], S. Siddhanta[52], T. Siemiarczuk[77], T.F. Silva[108], D. Silvermyr[73], T. Simantathammakul[103], R. Simeonov[35], B. Singh[89], B. Singh[93], K. Singh[48], R. Singh[78], R. Singh[54,95], S. Singh[15], V.K. Singh[132], V. Singhal[132], T. Sinha[97], B. Sitar[13], M. Sitta[130,56], T.B. Skaali[19], G. Skorodumovs[92], N. Smirnov[135], R.J.M. Snellings[59], E.H. Solheim[19], C. Sonnabend[32,95], J.M. Sonneveld[82], F. Soramel[27], A.B. Soto-Hernandez[86], R. Spijkers[82], I. Sputowska[105], J. Staa[73], J. Stachel[92], I. Stan[63], T. Stellhorn[123], S.F. Stiefelmaier[92], D. Stocco[101], I. Storehaug[19], N.J. Strangmann[64], P. Stratmann[123], S. Strazzi[25], A. Sturniolo[30,53], C.P. Stylianidis[82], A.A.P. Suaide[108], C. Suire[128], A. Suiu[32,111], M. Sukhanov[138], M. Suljic[32], R. Sultanov[138], V. Sumberia[89], S. Sumowidagdo[80], N.B.Sundstrom[59], L.H. Tabares[7], S.F. Taghavi[93], J. Takahashi[109], G.J. Tambave[78], Z. Tang[117], J. Tanwar[88], J.D. Tapia Takaki[115], N. Tapus[111], L.A. Tarasovicova[36], M.G. Tarzila[45], A. Tauro[32], A. Tavira García[128], G. Tejeda Muñoz[44], L. Terlizzi[24], C. Terrevoli[50], D. Thakur[24],

S. Thakur [4], M. Thogersen [19], D. Thomas [106], A. Tikhonov [138], N. Tiltmann [32,123], A.R. Timmins [113], A. Toia [64], R. Tokumoto[90], S. Tomassini [25], K. Tomohiro[90], N. Topilskaya [138], M. Toppi [49], V.V. Torres [101], A. Trifiró [30,53], T. Triloki [94], A.S. Triolo [32,53], S. Tripathy [32], T. Tripathy [124], S. Trogolo [24], V. Trubnikov [3], W.H. Trzaska [114], T.P. Trzcinski [133], C. Tsolanta[19], R. Tu[39], A. Tumkin [138], R. Turrisi [54], T.S. Tveter [19], K. Ullaland [20], B. Ulukutlu [93], S. Upadhyaya [105], A. Uras [125], M. Urioni [23], G.L. Usai [22], M. Vaid[89], M. Vala [36], N. Valle [55], L.V.R. van Doremalen[59], M. van Leeuwen [82], C.A. van Veen [92], R.J.G. van Weelden [82], D. Varga [46], Z. Varga [135], P. Vargas Torres[65], M. Vasileiou [76], A. Vasiliev [I,138], O. Vázquez Doce [49], O. Vazquez Rueda [113], V. Vechernin [138], P. Veen [127], E. Vercellin [24], R. Verma [47], R. Vértesi [46], M. Verweij [59], L. Vickovic[33], Z. Vilakazi[120], O. Villalobos Baillie [98], A. Villani [23], A. Vinogradov [138], T. Virgili [28], M.M.O. Virta [114], A. Vodopyanov [139], B. Volkel [32], M.A. Völkl [98], S.A. Voloshin [134], G. Volpe [31], B. von Haller [32], I. Vorobyev [32], N. Vozniuk [138], J. Vrláková [36], J. Wan[39], C. Wang [39], D. Wang [39], Y. Wang [39], Y. Wang [6], Z. Wang [39], A. Wegrzynek [32], F. Weiglhofer [38], S.C. Wenzel [32], J.P. Wessels [123], P.K. Wiacek [2], J. Wiechula [64], J. Wikne [19], G. Wilk [77], J. Wilkinson [95], G.A. Willems [123], B. Windelband [92], M. Winn [127], J. Witte [95], M. Wojnar [2], J.R. Wright [106], C.-T. Wu [6,27], W. Wu[39], Y. Wu [117], K. Xiong[39], Z. Xiong[117], L. Xu [6], R. Xu [6], A. Yadav [42], A.K. Yadav [132], Y. Yamaguchi [90], S. Yang [58], S. Yang [20], S. Yano [90], E.R. Yeats[18], J. Yi [6], R. Yin[39], Z. Yin [6], I.-K. Yoo [16], J.H. Yoon [58], H. Yu [12], S. Yuan[20], A. Yuncu [92], V. Zaccolo [23], C. Zampolli [32], F. Zanone [92], N. Zardoshti [32], P. Závada [62], M. Zhalov [138], B. Zhang [92], C. Zhang [127], L. Zhang [39], M. Zhang [124,6], M. Zhang [27,6], S. Zhang [39], X. Zhang [6], Y. Zhang[117], Y. Zhang [117], Z. Zhang [6], M. Zhao [10], V. Zherebchevskii [138], Y. Zhi[10], D. Zhou [6], Y. Zhou [81], J. Zhu [54,6], S. Zhu[95,117], Y. Zhu[6], S.C. Zugravel [56], N. Zurlo [131,55]

[1] *A.I. Alikhanyan National Science Laboratory (Yerevan Physics Institute) Foundation, Yerevan, Armenia*
[2] *AGH University of Krakow, Cracow, Poland*
[3] *Bogolyubov Institute for Theoretical Physics, National Academy of Sciences of Ukraine, Kiev, Ukraine*
[4] *Bose Institute, Department of Physics and Centre for Astroparticle Physics and Space Science (CAPSS), Kolkata, India*
[5] *California Polytechnic State University, San Luis Obispo, California, United States*
[6] *Central China Normal University, Wuhan, China*
[7] *Centro de Aplicaciones Tecnológicas y Desarrollo Nuclear (CEADEN), Havana, Cuba*
[8] *Centro de Investigación y de Estudios Avanzados (CINVESTAV), Mexico City and Mérida, Mexico*
[9] *Chicago State University, Chicago, Illinois, United States*
[10] *China Nuclear Data Center, China Institute of Atomic Energy, Beijing, China*
[11] *China University of Geosciences, Wuhan, China*
[12] *Chungbuk National University, Cheongju, Republic of Korea*
[13] *Comenius University Bratislava, Faculty of Mathematics, Physics and Informatics, Bratislava, Slovak Republic*
[14] *Creighton University, Omaha, Nebraska, United States*
[15] *Department of Physics, Aligarh Muslim University, Aligarh, India*
[16] *Department of Physics, Pusan National University, Pusan, Republic of Korea*
[17] *Department of Physics, Sejong University, Seoul, Republic of Korea*
[18] *Department of Physics, University of California, Berkeley, California, United States*
[19] *Department of Physics, University of Oslo, Oslo, Norway*
[20] *Department of Physics and Technology, University of Bergen, Bergen, Norway*
[21] *Dipartimento di Fisica, Università di Pavia, Pavia, Italy*

[22] *Dipartimento di Fisica dell'Università and Sezione INFN, Cagliari, Italy*
[23] *Dipartimento di Fisica dell'Università and Sezione INFN, Trieste, Italy*
[24] *Dipartimento di Fisica dell'Università and Sezione INFN, Turin, Italy*
[25] *Dipartimento di Fisica e Astronomia dell'Università and Sezione INFN, Bologna, Italy*
[26] *Dipartimento di Fisica e Astronomia dell'Università and Sezione INFN, Catania, Italy*
[27] *Dipartimento di Fisica e Astronomia dell'Università and Sezione INFN, Padova, Italy*
[28] *Dipartimento di Fisica 'E.R. Caianiello' dell'Università and Gruppo Collegato INFN, Salerno, Italy*
[29] *Dipartimento DISAT del Politecnico and Sezione INFN, Turin, Italy*
[30] *Dipartimento di Scienze MIFT, Università di Messina, Messina, Italy*
[31] *Dipartimento Interateneo di Fisica 'M. Merlin' and Sezione INFN, Bari, Italy*
[32] *European Organization for Nuclear Research (CERN), Geneva, Switzerland*
[33] *Faculty of Electrical Engineering, Mechanical Engineering and Naval Architecture, University of Split, Split, Croatia*
[34] *Faculty of Nuclear Sciences and Physical Engineering, Czech Technical University in Prague, Prague, Czech Republic*
[35] *Faculty of Physics, Sofia University, Sofia, Bulgaria*
[36] *Faculty of Science, P.J. Šafárik University, Košice, Slovak Republic*
[37] *Faculty of Technology, Environmental and Social Sciences, Bergen, Norway*
[38] *Frankfurt Institute for Advanced Studies, Johann Wolfgang Goethe-Universität Frankfurt, Frankfurt, Germany*
[39] *Fudan University, Shanghai, China*
[40] *Gangneung-Wonju National University, Gangneung, Republic of Korea*
[41] *Gauhati University, Department of Physics, Guwahati, India*
[42] *Helmholtz-Institut für Strahlen- und Kernphysik, Rheinische Friedrich-Wilhelms-Universität Bonn, Bonn, Germany*
[43] *Helsinki Institute of Physics (HIP), Helsinki, Finland*
[44] *High Energy Physics Group, Universidad Autónoma de Puebla, Puebla, Mexico*
[45] *Horia Hulubei National Institute of Physics and Nuclear Engineering, Bucharest, Romania*
[46] *HUN-REN Wigner Research Centre for Physics, Budapest, Hungary*
[47] *Indian Institute of Technology Bombay (IIT), Mumbai, India*
[48] *Indian Institute of Technology Indore, Indore, India*
[49] *INFN, Laboratori Nazionali di Frascati, Frascati, Italy*
[50] *INFN, Sezione di Bari, Bari, Italy*
[51] *INFN, Sezione di Bologna, Bologna, Italy*
[52] *INFN, Sezione di Cagliari, Cagliari, Italy*
[53] *INFN, Sezione di Catania, Catania, Italy*
[54] *INFN, Sezione di Padova, Padova, Italy*
[55] *INFN, Sezione di Pavia, Pavia, Italy*
[56] *INFN, Sezione di Torino, Turin, Italy*
[57] *INFN, Sezione di Trieste, Trieste, Italy*
[58] *Inha University, Incheon, Republic of Korea*
[59] *Institute for Gravitational and Subatomic Physics (GRASP), Utrecht University/Nikhef, Utrecht, Netherlands*
[60] *Institute of Experimental Physics, Slovak Academy of Sciences, Košice, Slovak Republic*
[61] *Institute of Physics, Homi Bhabha National Institute, Bhubaneswar, India*
[62] *Institute of Physics of the Czech Academy of Sciences, Prague, Czech Republic*
[63] *Institute of Space Science (ISS), Bucharest, Romania*
[64] *Institut für Kernphysik, Johann Wolfgang Goethe-Universität Frankfurt, Frankfurt, Germany*
[65] *Instituto de Ciencias Nucleares, Universidad Nacional Autónoma de México, Mexico City, Mexico*
[66] *Instituto de Física, Universidade Federal do Rio Grande do Sul (UFRGS), Porto Alegre, Brazil*
[67] *Instituto de Física, Universidad Nacional Autónoma de México, Mexico City, Mexico*
[68] *iThemba LABS, National Research Foundation, Somerset West, South Africa*
[69] *Jeonbuk National University, Jeonju, Republic of Korea*

[70] *Johann-Wolfgang-Goethe Universität Frankfurt Institut für Informatik, Fachbereich Informatik und Mathematik, Frankfurt, Germany*
[71] *Laboratoire de Physique Subatomique et de Cosmologie, Université Grenoble-Alpes, CNRS-IN2P3, Grenoble, France*
[72] *Lawrence Berkeley National Laboratory, Berkeley, California, United States*
[73] *Lund University Department of Physics, Division of Particle Physics, Lund, Sweden*
[74] *Nagasaki Institute of Applied Science, Nagasaki, Japan*
[75] *Nara Women's University (NWU), Nara, Japan*
[76] *National and Kapodistrian University of Athens, School of Science, Department of Physics, Athens, Greece*
[77] *National Centre for Nuclear Research, Warsaw, Poland*
[78] *National Institute of Science Education and Research, Homi Bhabha National Institute, Jatni, India*
[79] *National Nuclear Research Center, Baku, Azerbaijan*
[80] *National Research and Innovation Agency - BRIN, Jakarta, Indonesia*
[81] *Niels Bohr Institute, University of Copenhagen, Copenhagen, Denmark*
[82] *Nikhef, National institute for subatomic physics, Amsterdam, Netherlands*
[83] *Nuclear Physics Group, STFC Daresbury Laboratory, Daresbury, United Kingdom*
[84] *Nuclear Physics Institute of the Czech Academy of Sciences, Husinec-Řež, Czech Republic*
[85] *Oak Ridge National Laboratory, Oak Ridge, Tennessee, United States*
[86] *Ohio State University, Columbus, Ohio, United States*
[87] *Physics department, Faculty of science, University of Zagreb, Zagreb, Croatia*
[88] *Physics Department, Panjab University, Chandigarh, India*
[89] *Physics Department, University of Jammu, Jammu, India*
[90] *Physics Program and International Institute for Sustainability with Knotted Chiral Meta Matter (WPI-SKCM^2), Hiroshima University, Hiroshima, Japan*
[91] *Physikalisches Institut, Eberhard-Karls-Universität Tübingen, Tübingen, Germany*
[92] *Physikalisches Institut, Ruprecht-Karls-Universität Heidelberg, Heidelberg, Germany*
[93] *Physik Department, Technische Universität München, Munich, Germany*
[94] *Politecnico di Bari and Sezione INFN, Bari, Italy*
[95] *Research Division and ExtreMe Matter Institute EMMI, GSI Helmholtzzentrum für Schwerionenforschung GmbH, Darmstadt, Germany*
[96] *Saga University, Saga, Japan*
[97] *Saha Institute of Nuclear Physics, Homi Bhabha National Institute, Kolkata, India*
[98] *School of Physics and Astronomy, University of Birmingham, Birmingham, United Kingdom*
[99] *Sección Física, Departamento de Ciencias, Pontificia Universidad Católica del Perú, Lima, Peru*
[100] *Stefan Meyer Institut für Subatomare Physik (SMI), Vienna, Austria*
[101] *SUBATECH, IMT Atlantique, Nantes Université, CNRS-IN2P3, Nantes, France*
[102] *Sungkyunkwan University, Suwon City, Republic of Korea*
[103] *Suranaree University of Technology, Nakhon Ratchasima, Thailand*
[104] *Technical University of Košice, Košice, Slovak Republic*
[105] *The Henryk Niewodniczanski Institute of Nuclear Physics, Polish Academy of Sciences, Cracow, Poland*
[106] *The University of Texas at Austin, Austin, Texas, United States*
[107] *Universidad Autónoma de Sinaloa, Culiacán, Mexico*
[108] *Universidade de São Paulo (USP), São Paulo, Brazil*
[109] *Universidade Estadual de Campinas (UNICAMP), Campinas, Brazil*
[110] *Universidade Federal do ABC, Santo Andre, Brazil*
[111] *Universitatea Nationala de Stiinta si Tehnologie Politehnica Bucuresti, Bucharest, Romania*
[112] *University of Derby, Derby, United Kingdom*
[113] *University of Houston, Houston, Texas, United States*
[114] *University of Jyväskylä, Jyväskylä, Finland*
[115] *University of Kansas, Lawrence, Kansas, United States*
[116] *University of Liverpool, Liverpool, United Kingdom*
[117] *University of Science and Technology of China, Hefei, China*
[118] *University of South-Eastern Norway, Kongsberg, Norway*

JHEP11(2025)076

[119] *University of Tennessee, Knoxville, Tennessee, United States*
[120] *University of the Witwatersrand, Johannesburg, South Africa*
[121] *University of Tokyo, Tokyo, Japan*
[122] *University of Tsukuba, Tsukuba, Japan*
[123] *Universität Münster, Institut für Kernphysik, Münster, Germany*
[124] *Université Clermont Auvergne, CNRS/IN2P3, LPC, Clermont-Ferrand, France*
[125] *Université de Lyon, CNRS/IN2P3, Institut de Physique des 2 Infinis de Lyon, Lyon, France*
[126] *Université de Strasbourg, CNRS, IPHC UMR 7178, F-67000 Strasbourg, France*
[127] *Université Paris-Saclay, Centre d'Etudes de Saclay (CEA), IRFU, Départment de Physique Nucléaire (DPhN), Saclay, France*
[128] *Université Paris-Saclay, CNRS/IN2P3, IJCLab, Orsay, France*
[129] *Università degli Studi di Foggia, Foggia, Italy*
[130] *Università del Piemonte Orientale, Vercelli, Italy*
[131] *Università di Brescia, Brescia, Italy*
[132] *Variable Energy Cyclotron Centre, Homi Bhabha National Institute, Kolkata, India*
[133] *Warsaw University of Technology, Warsaw, Poland*
[134] *Wayne State University, Detroit, Michigan, United States*
[135] *Yale University, New Haven, Connecticut, United States*
[136] *Yildiz Technical University, Istanbul, Turkey*
[137] *Yonsei University, Seoul, Republic of Korea*
[138] *Affiliated with an institute formerly covered by a cooperation agreement with CERN*
[139] *Affiliated with an international laboratory covered by a cooperation agreement with CERN*

[I] *Deceased*
[II] *Also at: Max-Planck-Institut fur Physik, Munich, Germany*
[III] *Also at: Italian National Agency for New Technologies, Energy and Sustainable Economic Development (ENEA), Bologna, Italy*
[IV] *Also at: Instituto de Fisica da Universidade de Sao Paulo*
[V] *Also at: Dipartimento DET del Politecnico di Torino, Turin, Italy*
[VI] *Also at: Department of Applied Physics, Aligarh Muslim University, Aligarh, India*
[VII] *Also at: Institute of Theoretical Physics, University of Wroclaw, Poland*
[VIII] *Also at: Facultad de Ciencias, Universidad Nacional Autónoma de México, Mexico City, Mexico*

JHEP11(2025)076